Improved noise bias compensation-equivalent circuit modeling strategy for battery state of charge estimation adaptive to strong electromagnetic interference.

YANG, X., WANG, S., TAKYI-ANINAKWA, P., YANG, X. and FERNANDEZ, C.

2023

Improved noise bias compensation-equivalent circuit modeling strategy for battery state of charge estimation adaptive to strong electromagnetic interference

Xiaoyong Yang[1], Shunli Wang[1,2*], Paul Takyi-Aninakwa[1], Xiao Yang[1], Carlos Fernandez[3]

[1] School of Information Engineering, Southwest University of Science and Technology, Mianyang 621010, China; [2] College of Electrical Engineering, Sichuan University, Chengdu 610065, China; [3] School of Pharmacy and Life Sciences, Robert Gordon University, Aberdeen AB10-7GJ, UK.

Abstract: Strong electromagnetic interference, which has a significant impact on the performance and safety of the lithium-ion battery, usually affects the accurate state of charge (SOC). Different optimization strategies are used to estimate the model parameters and the SOC due to the unknown nonlinear characteristics caused by noise. However, the impact of sensor and model errors is treated separately. To express the sensor and model uncertainties, a noise bias compensation-equivalent circuit model (NBC-ECM) is proposed, in which sensor noise and model error voltages are employed in the model structure and the SOC estimation process of the lithium-ion battery. For parameter identification, a singular value decomposition-bias compensation recursive least squares (SVD-BCRLS) algorithm is proposed to identify the characteristic micro-parameters of the battery. Then, a moving window adaptive extended Kalman filtering (MWAEKF) algorithm based on window functions is proposed for accurate SOC estimation of lithium-ion batteries. The stability of the model parameters and the reliability of the proposed algorithm in estimating the SOC are evaluated using different noise factors: current and voltage sensor noises of 10 and 50 mA. Using the proposed SVD-BCRLS-MWAEKF algorithm, the maximum SOC error is 1.3%, the root mean square error (RMSE) is 0.3972%, and the mean absolute error (MAE) is 0.2316% using the noise of 0.05 V/A under the hybrid power pulse characterization (HPPC) operating condition. With the same noise value under the Beijing bus dynamic stress test (BBDST) operating condition, the proposed algorithm SOC has a maximum SOC error of 1.57%, an RMSE of 0.5638%, and an MAE of 0.4475%. Under noise interference conditions, estimation is more accurate compared to static conditions, proving that the proposed algorithm can overcome the uncertainties encountered by lithium-ion batteries for real-time BMS applications.

Keywords: State of charge; Lithium-ion battery; Noise bias compensation-equivalent circuit model; Singular value decomposition-bias compensation recursive least squares; Moving window adaptive extended Kalman filter

***Corresponding author**: Shunli Wang. E-mail address: wangshunli1985@qq.com.

1. Introduction

Because of the limitations of fossil energy and its associated global warming effects, the electric vehicle (EV) market has experienced unprecedented growth, with electricity serving as a driving force from renewable and clean energy sources [1]. Lithium-ion batteries are increasingly powering our world through EVs and energy storage systems [2]. It is due to their unique properties, such as high energy density, lightweight, long cycle life, low self-discharge rate, no memory effect, etc. [3-6]. However, an effective battery management system (BMS) is necessary for EVs to guarantee reliable, safe, and stable power delivery for the various devices for which these batteries provide energy under different conditions [7, 8]. Among the functions of the BMS is the estimation of the state of charge (SOC), which is a measure of stored electricity, and its estimation attracts broad attention [9]. As only current, voltage, and sometimes surface temperature are measured by the BMS for SOC estimation, estimating internal battery states becomes an urgent topic to avoid any overcharging and over-discharging of the EV's battery for safe and long-lasting operation [10, 11].

1.1. *Literature review*

As a critical battery state parameter, the SOC serves as a reference for the BMS's safe and reliable operation [12]. It cannot, however, be measured directly and must be estimated using efficient and accurate methods. Several methods have been proposed in recent times, and these methods can be divided into four categories, which include direct measurement methods, open-circuit voltage (OCV) method, data-driven methods, and model-based methods [13]. The direct measurement methods for SOC estimation of lithium-ion batteries are constructed based on the characterization of the battery parameters, which includes Ampere-hour (Ah) integral [14], electrochemical impedance spectroscopy [15], and internal resistance [16] methods. However, as simply and easily as these methods can be implemented on the BMS, they are highly susceptible to the uncertainties of the operating conditions, which

affect their estimation accuracy and robustness [17]. The OCV method is used to estimate the SOC based on the approximate OCV-SOC linear relationship [18]. However, since the SOC of a lithium-ion battery is related to the embedding quantity in the active material, an OCV method can estimate the SOC after the battery gets sufficient rest to reach equilibrium, which may be two hours in some cases, resulting in much inconvenience [16, 19]. Data-driven methods such as the gated recurrent unit [20], long short-term memory [21], convolutional neural network [22], nonlinear autoregressive model with exogenous input [23], etc., have been proposed for SOC estimation of lithium-ion batteries. However, one of the major limitations of these methods is that they operate as a "black box", which makes it difficult to explain certain results and determine the root cause [24]. Furthermore, converged training results at various local optimum levels with random weight initialization could result in different performances and computational costs for batteries under new operating conditions, resulting in an overall trial-and-error network training process, making it less attractive for battery state estimation, especially when the cause of the results is also difficult to explain [25]. Moreover, due to the large training sample requirement, it has a high computational demand [26].

In comparison to prior methods, model-based methods achieve successful application due to the rational trade-off between computation cost and estimation accuracy. In this SOC estimation process, the error source mainly exists in two parts: the imprecise battery model and an estimation algorithm. As one of the battery models, the equivalent circuit model (ECM) serves as the core element of the BMS and has been widely used to simulate the nonlinear characteristic parameters of the battery using circuit elements and linear parameter changes [27, 28]. The model's quality determines whether the battery can operate safely and reliably over time. However, the performance of the model highly depends on the model's structure to simulate these dynamic characteristics of the battery by effectively determining the trade-off between computational complexity and accuracy for SOC estimation of the battery [29-31]. To use this class of method, battery model parameters must be identified for the state estimation algorithm, which may be identified offline or online. The offline parameter identification method uses least-squares curve fitting to identify the parameters of the battery [32]. However, they do not have real-time adaptability due to changes in the

operating environment, and only point-to-point parameters are available [33]. The online parameter identification can adaptively accommodate and adapt to the complex operating conditions of the battery. Typically, the recursive least squares (RLS) method is used to minimize the sum of the calculation error squares when autonomously identifying the battery parameters for state estimation methods [34-36].

Kalman filter-based algorithms, such as extended Kalman filter (EKF), unscented Kalman filter (UKF) [37-39], cubature Kalman filter (CKF) [40], sigma-point Kalman filter (SPKF) [41, 42], etc., are established based on the different variants of the ECMs and are suitable for SOC estimation of lithium-ion batteries. For instance, given the possibility of divergence caused by inaccurate initial covariance matrices, He et al. [43] used the AEKF algorithm to adaptively update process and measurement noise covariance matrices to improve estimation accuracy even further. Peng et al. [44] proposed an improved adaptive dual UKF algorithm to achieve co-estimation for battery model parameters and SOC, where the algorithm estimates the SOC precisely under some interferences, such as an erroneous initial SOC, inaccurate battery capacity, and different ambient temperatures. Li et al. [45] proposed using a sequential Monte Carlo filter with EKF to determine the cell SOC and its electrochemical impedance, which refines the treatment of hysteresis voltage using the probability density function (PDF) with an online adaptation of its model parameters. Tong et al. [46] proposed an improved UKF to estimate the SOC that includes the use of nonlinear state-space models to reduce random measurement loss and inaccurate noise covariance matrices to reflect the uncertainties. Bhattacharyya et al. [47] used EKF and DEKF methods for the on-road SOC estimation of lithium-ion batteries, where the impact of voltage and current sensor bias on SOC is investigated. Xu et al. [48] proposed a novel dual fuzzy-based adaptive extended Kalman filter (DFAEKF) method for the SOC estimation of lithium metal batteries, which designs an intelligent noise estimator based on a fuzzy inference system to adjust the length of the residual innovation sequence to update the noise covariance. Maheshwari et al. [49] proposed a sunflower optimization with an EKF algorithm to find the optimal values of the process and measurement noise covariance matrices. To address the problem, improving battery SOC estimation with noise bias characterization has great potential. The polynomial regression and the Gaussian process regression models are proposed to examine the effects of the two methods based

on a noise bias model [50].

However, in the actual operating conditions, the complexity of the internal nonlinear structure of the battery and the uncertainties make the estimation model and algorithm of the actual state of the battery encounter many challenges by not taking into account the estimation accuracy being affected by external noise under correspondingly complex operating conditions [51]. From the battery model to the estimation algorithm, any aspect of research is inevitably linked to determining the estimation accuracy. Therefore, under complex operating conditions, it is essential to estimate the noise so that the system can be considered uniform. Because of the sensitivity of current detection, noise introduces errors into the model via limited current sensor resolution and entering current data while subject to electromagnetic interference. The contamination of current data affects the identification of model parameters in terms of model-matching adaptability. As a result, the voltage noise generated by the current passing through the battery system must be considered, as it affects the accuracy of the SOC.

1.2. *Objectives of this paper*

Considering the influence of the first-order Thevenin ECM, its trade-off between computational complexity and accuracy, and the influence of noise in the whole process of SOC estimation, this paper proposes the idea of using an independent noise bias model to simulate the error characteristics of the battery model by employing bias compensation and augmented matrix methods to complete the model's construction. The objectives of this paper are in two folds:

(1) A noise bias compensation (NBC)-ECM is proposed using the extracted state noise to compensate for the ECM state error, in which the current fluctuation and voltage error of the battery are fully considered, where the current fluctuation may be affected by different amplitudes of Gaussian white noise and colored noise.

(2) A singular value decomposition-bias compensation recursive least squares and moving window adaptive extended Kalman filtering (SVD-BCRLS-MWAEKF) functional algorithm is proposed for the dynamic parameter identification and SOC estimation. The hybrid power pulse characterization (HPPC) test and Beijing bus dynamic stress test (BBDST) operating conditions are considered to verify the accuracy and robustness of the algorithm.

2. Development of battery modeling and SOC methods

2.1. *Noise bias compensation-equivalent circuit modeling method*

In a typical battery system, the ECM of the battery can realize the complete equivalent of the external characteristics of the battery. During battery discharge, the current and voltage fluctuations caused by changes in the strong electromagnetic interference are transmitted to the ECM via the sensor, which makes SOC estimation difficult. Therefore, it is reasonable and effective to develop an NBC-ECM based on a current fluctuation whose state noise is conditioned by observation noise. Considering the problem of parameter coupling and noise interference, the first-order RC ECM is employed as a base model to establish the NBC-ECM by adding a system structure function to compensate for the noise interference, whose architecture is shown in Figure 1.

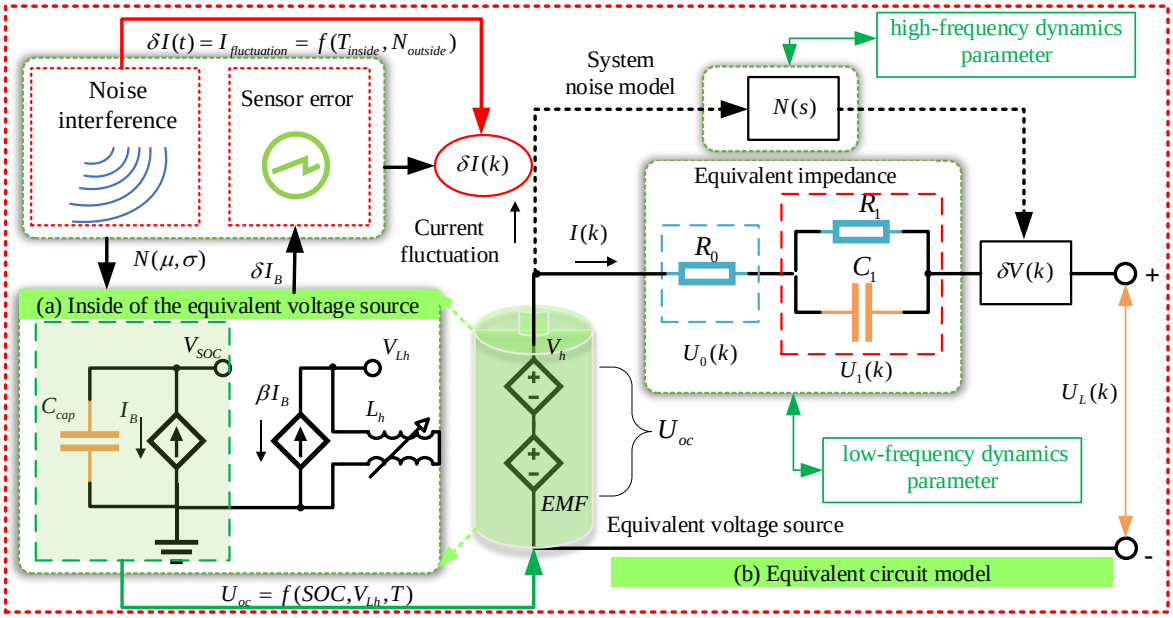

Figure 1. The architecture of the noise bias compensation-equivalent circuit model

As shown in Figure 1, the NBC-ECM consists of complex components: (a) the internal component of the equivalent voltage source and: (b) the battery ECM. In Subfigure 1(a), the equivalent voltage source section for the lithium-ion battery is shown, and C_{cap} is the capacitance of the battery. The current I_B flows through the capacitance C_{cap} to obtain the SOC by accumulating charge, which is the original expression of the ampere-hour integration method. Then, I_B is amplified by a magnification factor β to produce the inductive voltage V_{Lh} that controls the hysteretic voltage V_h, as relationally expressed in Equation (1).

$$\begin{cases} V_h = f(V_{soc}, V_{Lh}) \\ EMF = f(V_{soc}) \\ U_{oc} = V_h + EMF \end{cases} \tag{1}$$

In Equation (1), U_{oc} is the open-circuit voltage (OCV), the hysteresis voltage V_h is mainly determined by the inductance V_{Lh} and SOC, the EMF is mainly determined by SOC. It is worth noting that the EMF is the electromotive force of the battery obtained under noiseless conditions, while the V_h has different performance because of the change in different current I_B operating conditions. When current fluctuation δI_B is considered as the factor of the U_{oc} variation, its effect can be expressed by Equation (2).

$$\delta U_{oc} = f(\delta I_B) \tag{2}$$

In Equation (2), the δU_{oc} is controlled by current fluctuation δI_B. Among them, the δEMF is affected by the change of the SOC which depends on the value of δI_B, and the δV_h is affected by the change of SOC and δV_{Lh} which depends on the δI_B through the amplification of the coefficient β .

Due to the limited accuracy of the sensor detection, there is often a certain degree of current fluctuation value $\delta I(k)$ during the use of the sensor, depending on the battery system. The input value of the current is shown in Equation (3).

$$I_L = I(k) + \delta I(k) \tag{3}$$

In Equation (3), the total current I_L consists of the real-time measurement current $I(k)$ flowing out of the battery and the current fluctuations $\delta I(k)$ caused by sensor noise. Therefore, the Ah integration is performed to obtain the reference SOC using the real current data. As a representation of the residual energy in the battery, the SOC is calculated using Equation (4).

$$SOC(k) = SOC(k_0) - \frac{1}{C_{cap}} \int_{k_0}^{k} \eta \cdot \big(I(k) + \delta I(k)\big)\, dk \tag{4}$$

As is shown in Equation (4), C_{cap} denotes the actual capacity of the battery, η denotes the Coulombic efficiency of the battery, which is set to 1, and k_0 represents the initial SOC time. The SOC is obtained by the Ah integral method of the total current. From the internal complex equivalent circuit in Figure 1(a), it is easy to see that when sensor noise enters the battery model through the current, it is reflected not only in the value of SOC by the Ah integration in Equation (4) but also in the change of direction through the inductor change V_{Lh} in OCV in Equation

(2). Consequently, the ECM is shown in Subfigure 1(b). Based on Kirchhoff's circuit law and capacitance characteristics, the continuous state-space equation is obtained, as shown in Equation (5).

$$\begin{cases} U_{oc}(k) = I(k)R_0 + U_1(k) + U_L(k) + \delta \mathrm{V}(k) \\ \delta V(k) = \mathrm{N}(z^{-1})\delta I(k) \\ U_1(k) = (1 - e^{-\frac{k}{R_1C_1}})I(k)R_1 + e^{-\frac{k}{R_1C_1}}U(0) \end{cases} \tag{5}$$

From Figure 1 and Equation (5), the value of the voltage source is considered equal to the OCV $U_{oc}(k)$, which is determined by the current SOC value. $U_1(k)$ represents the voltage drops across the RC circuit, $U_L(k)$ is the measured voltage, and $U_{oc}(k)$ is obtained through the curve-fitting relationship of $U_{oc} = f(SOC, V_{Lh})$. The R_0 represents the internal ohmic resistance. The electrochemical polarization resistor R_1 and polarization capacitor C_1 is used to simulate the low-frequency dynamic parameter characteristics of the lithium-ion battery. It is worth noting that the impedance network formed by these three parameters varies very little with the SOC of the battery and has a slowly changing value. Compared to the equivalent impedance network, the surge of voltage obtained from the current fluctuation through the noisy system module varies sharply, which is a rapidly changing value used to reflect the high-frequency dynamics parameter characteristics of the lithium-ion battery.

2.2. *Model-based discrete state-space representation*

When noise is present in the model, SOC, as a state parameter reflecting the remaining capacity of the battery, affects its accuracy. Therefore, it is a critical parameter to be considered for the state changes of the battery. Usually, the SOC is obtained using the Ah integration. However, under experimental conditions, the use of its expression changes from Equations (4) to (6).

$$z_k = z_0 + \frac{\sum_{k=0}^{N} I_k}{C_{cap}} \Delta k + \frac{\sum_{k=0}^{N} \delta I_k}{C_{cap}} \Delta k \tag{6}$$

In Equation (6), z_k and z_0 represent the SOC value at time steps k and 0, respectively. Δk is the sampling time of the BMS and I_k is the input current of the battery at the time step k.

In Section 2.1, it can be observed that U_{oc} is affected by SOC and V_{Lh}, while the current I_B also indirectly affects U_{oc} through its variation factor δI_B. However, V_h and EMF expressions with z_k cannot be obtained independently using Equation (1) but can be obtained using Equation (7).

$$\begin{cases} V_{EMF,k}(z_k) = \sum_{k=0}^{N} \left(OCV_{ch,i,k}(z_k) + OCV_{dis,k}(z_k)\right)/2N \\ V_{h,k}(z_k) = \sum_{k=0}^{N} \left(OCV_{ch,i,k}(z_k) - OCV_{dis,k(z_k)}(z_k)\right)/2N \end{cases} \tag{7}$$

In Equation (7), $V_{EMF,k}$ and $V_{h,k}$ represent the values of the EMF and hysteresis voltage, respectively, at time step k.The $OCV_{ch,i,k}$ and $OCV_{dis,k}$ represent the OCV at the charging and discharging moment of the ith iteration at time step k, and N represents the length of the selected sample. It is worth noting that the effect of the parameters caused by the current variation can only be represented by the noise model, as shown in Equation (8).

$$U_{L,k} = \underbrace{\underbrace{V_{EMF,k}(z_k) + V_{h,k}(z_k)}_{U_{oc,k}(z_k)} + \underbrace{\underbrace{\delta V_k(\delta I_k)}_{\delta U_{oc,k}(z_k)}}_{high-frequency} + \underbrace{U_{1,k} - R_0 I_k}_{low-frequency}}_{} \tag{8}$$

According to the above-mentioned analyses of the OCV, hysteresis voltage, and equivalent impedance voltage in the NBC-ECM, the state-space and observation equations based on the battery model are in Equation (9).

$$\begin{bmatrix} z_k \\ U_{1,k} \\ \delta V_k \end{bmatrix} = \begin{bmatrix} 1 & 0 & 0 \\ 0 & e^{-\frac{\Delta k}{R_1 C_1}} & 0 \\ 0 & 0 & \Pi_{k,k-1} \end{bmatrix} \begin{bmatrix} z_{k-1} \\ U_{1,k-1} \\ \delta V_{k-1} \end{bmatrix} + \begin{bmatrix} \frac{\Delta k}{C_{cap}} \\ R_1(1 - e^{-\frac{\Delta k}{R_1 C_1}}) \\ 0 \end{bmatrix} I_k + \begin{bmatrix} \frac{\Delta k}{C_{cap}} \\ 0 \\ 1 \end{bmatrix} \delta I_k \tag{9}$$

As is shown in Equation (9), it is worth noting that δV_k, as the noise state inside the cell, is not only related to the noise model function $\Pi_{k,k-1}$, but also to the system noise δI_k. This result also reflects the effect of δI_k in the battery, as shown in Equation (1).

2.3 The SVD-BCRLS parameter identification method

In conventional battery models, only two variables, current and voltage, are considered in the parameter identification, and the response mechanisms take two common observations into account during the charge and discharge states. Because the complex characteristics of the battery are frequently influenced by external factors, noise as an external input variable is a reality-based consideration. When the effects of environmental noise must be considered, the modeled characteristics of the battery in the presence of noise take precedence. Given the error in the sampled values of the data, the relationship between a set of true and measured values is expressed in Equation (10).

$$M_k = M_k^* + \Delta M + \delta M_k \tag{10}$$

In Equation (10), the measurement values M_k include the true value M_k^*, the constant bias ΔM, and the randomly varying δM_k. It is worth noting that constant bias ΔM and randomly varying part δM_k two components are of

particular concern. The noise effect is mainly from current noise and voltage noise. Assuming that the current error is $\xi_I(k)$, which is from the sensor noises and resolution effect, the voltage error is $\xi_V(k)$, which is from the model parameter error, fitting error of the OCV-SOC, and other related noise, the random noise is independent and identically distributed. The mean and variance are expressed, as respectively shown in Equation (11).

$$\begin{cases} E\big(\xi_I(k)\big) = E(\Delta I + \delta I_k) = \Delta I, \sigma^2(\xi_I(k)) = \sigma^2(\delta I_k) = \sigma_I^2 \\ E\big(\xi_V(k)\big) = E(\Delta V + \delta V_k) = \Delta V, \sigma^2(\xi_V(k)) = \sigma^2(\delta V_k) = \sigma_V^2 \end{cases} \tag{11}$$

In the Equation (11), the error characteristics of the current are represented by the mean $E\big(\xi_I(k)\big)$ and variance $\sigma^2\big(\xi_I(k)\big)$. Also, those of the voltage are represented by the mean $E\big(\xi_V(k)\big)$ and variance $\sigma^2(\xi_V(k))$. For the ΔM and δM_k, one of the more obvious differences is that the former is a constant deviation and will show a constant mean in the statistical properties of the error, while the latter is a random deviation and will show a certain variance in the statistical properties of the error. The actual relationship between a set of true and measured values is shown in Equation (12).

$$M_k = M(k) + \delta M_k \tag{12}$$

In Equation (12), $M(k)$ is a variable that varies in real time, contains the results of both M_k^* and ΔM, the resolution error and true values in the detection results of the current, the fitting error of the OCV, and true values in the detection results of the voltage. The noise variable is represented as an independent variable in δM_k.

When the influence of noise factors is added, the continuous model with added noise can be transformed from Equation (5) to (13).

$$\big(U_{oc}(s) - U_L(s)\big) + \delta V(s) = (I(s) + \delta I(s))R_0 + \frac{(I(s) + \delta I(s))R_1}{R_1 C_1 s + 1} \tag{13}$$

In the Equation (13), $\delta I(s)$ represents a small change in the input noise from current, and $\delta V(s)$ represents the output noise from the voltage that has the same structure as the system noise.

Using $s = \frac{2}{T}\frac{1-z^{-1}}{1+z^{-1}}$ to discretize Equation (13), then simplify and sort out $E(k) = U_L(k) - U_{oc}(k)$ to obtain Equation (14).

$$\begin{cases} E(k) + \delta V(k) = G(z^{-1})i(k) + N(z^{-1})\delta I(k) \\ G(z^{-1}) = \dfrac{E(k)}{I(k)} = \dfrac{\theta_2 + \theta_3 z^{-1}}{1 + \theta_1 z^{-1}} \\ N(z^{-1}) = \dfrac{\delta V(k)}{\delta I(k)} = \dfrac{\theta_4 + \theta_5 z^{-1}}{1 + \theta_1 z^{-1}} \end{cases} \tag{14}$$

In Equation (14), θ_1 represents the pole characteristics of the system. $\theta_2, \theta_3, \theta_4$, and θ_5 represents the zero characteristics of the system. Using a sum of $E(k)$ and $\delta V(k)$ as the value of the measured voltage $z(k)$, based on the system structure shown in Figure 1, the input parameter structure of the battery is constructed, as shown in Figure 2.

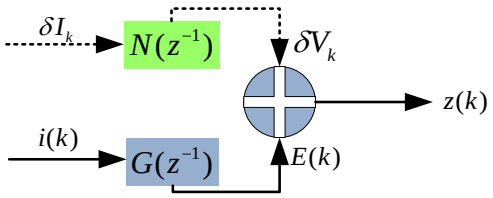

Figure 2. Structure of parameter identification based on NBC-ECM

In Figure 2, the outputs are represented using two system functions $G(z^{-1})$ and $N(z^{-1})$. By simplification, the parameter equation can be expressed, as shown in Equation (15).

$$\begin{cases} E(k) = \theta_1 E(k-1) + \theta_2 I(k) + \theta_3 I(k-1) \\ \delta V(k) = \theta_1 \delta V(k-1) + \theta_4 \delta I(k) + \theta_5 \delta I(k-1) \end{cases} \tag{15}$$

From Equation (15), the results of state noise can be obtained. Then, by combining the two equations in Equation (15), the identification function can be obtained, as shown in Equation (16) .

$$\begin{cases} z(k) = \theta_1 z(k-1) + \theta_2 I(k) + \theta_3 I(k-1) + \theta_4 \xi(k) + \theta_5 \xi(k-1) \\ \theta_1 = \dfrac{T - 2R_1C_1}{T + 2R_1C_1} \\ \theta_2 = \dfrac{R_0T + R_1T + 2R_1C_1R_0}{T + 2R_1C_1} \\ \theta_3 = \dfrac{R_0T + R_1T - 2R_1C_1R_0}{T + 2R_1C_1} \\ \theta_4 = noise\ factor(1) \\ \theta_5 = noise\ factor(2) \end{cases} \tag{16}$$

To obtain expressions for the identified parameters, Equation (16) is transformed into the discrete-time domain, as shown in Equation (17).

$$\begin{cases} z(k) = \boldsymbol{h}(k)^T \boldsymbol{\theta}(k) \\ \boldsymbol{h}(k) = [z(k-1) \quad I(k) \quad I(k-1) \quad \delta I(k) \quad \delta I(k-1)]^T \\ \boldsymbol{\theta}(k) = [\theta_1 \quad \theta_2 \quad \theta_3 \quad \theta_4 \quad \theta_5] \end{cases} \tag{17}$$

The model parameters R_0,R_1,C_1, and $N(z^{-1})$ are obtained using the SVD-BCRLS parameter identification algorithm. The detailed recursive process of the online parameter identification method includes five steps:

At time step $k = 0$:

Step 1: Initialization:

1. Initialization of identified parameter $\widehat{\boldsymbol{\theta}}(0)$ and error covariance matrix $\boldsymbol{P}(0)$, as shown in Equation (18).

$$\begin{cases} \widehat{\boldsymbol{\theta}}(0) = E[\boldsymbol{\theta}(0)] \\ \boldsymbol{P}(0) = E[(\widehat{\boldsymbol{\theta}}(0) - \boldsymbol{\theta}(0))(\widehat{\boldsymbol{\theta}}(0) - \boldsymbol{\theta}(0))^T] \end{cases} \tag{18}$$

2. Initialization of decomposition parameter $\boldsymbol{U}(0)$ and $\boldsymbol{D}(0)$, as shown in Equation (19).

$$\begin{cases} \boldsymbol{U}(0) = \boldsymbol{I} \\ \boldsymbol{D}(0) = \sqrt{\boldsymbol{P}(0)} \end{cases} \tag{19}$$

At the time $k = 1,2, \dots, N$, repeat:

Step 2: One-step update of the identified parameters $\widehat{\boldsymbol{\theta}}_{LS}(k)$, error residual $\boldsymbol{e}(k)$, and gain matrix $\boldsymbol{K}(k)$, as shown in Equation (20).

$$\begin{cases} \boldsymbol{e}(k) = \boldsymbol{z}(k) - \boldsymbol{h}^T(k)\widehat{\boldsymbol{\theta}}_{LS}(k-1) \\ \boldsymbol{K}(k) = \boldsymbol{P}(k-1)\boldsymbol{h}(k)[\lambda + \boldsymbol{h}^T(k)\boldsymbol{P}(k-1)\boldsymbol{h}(k)]^{-1} \\ \widehat{\boldsymbol{\theta}}_{LS}(k) = \widehat{\boldsymbol{\theta}}_{LS}(k-1) + \boldsymbol{K}(k)\boldsymbol{e}(k) \end{cases} \tag{20}$$

Step 3: One-step calculation of the error criterion function $\boldsymbol{J}(k)$ and bias compensation factor $\boldsymbol{\sigma}^2(k)$ using Equation (21).

$$\begin{cases} \boldsymbol{J}(k) = \boldsymbol{J}(k-1) + \dfrac{\boldsymbol{e}^2(k)}{1 + \boldsymbol{h}^T(k)\boldsymbol{P}(k-1)\boldsymbol{h}(k)} \\ \boldsymbol{\sigma}^2(k) = \dfrac{\boldsymbol{J}(k)}{k[1 + \boldsymbol{\theta}_{BC}(k-1)\boldsymbol{D}\boldsymbol{\theta}_{LS}(k-1)]} \end{cases} \tag{21}$$

Step 4: One-step error covariance matrix $\boldsymbol{P}(k)$ for the calculation of the SVD algorithm:

1. Update the construction matrix $\boldsymbol{\Sigma} \in \boldsymbol{R}^{(n+1)\times n}$ using Equation (22).

$$\boldsymbol{\Sigma} = \begin{bmatrix} \boldsymbol{h}^T(k)\boldsymbol{U}(k-1) \\ \boldsymbol{D}^{-1}(k-1) \end{bmatrix} = \bar{\boldsymbol{U}}(k-1)\begin{bmatrix} \bar{\boldsymbol{D}}(k-1) \\ 0 \end{bmatrix}[\bar{\boldsymbol{V}}(k-1)]^T \tag{22}$$

2. Construct the singular array $\boldsymbol{U}(k)$ and update the error covariance matrix $\boldsymbol{P}(k)$, as shown in Equation (23).

$$\begin{cases} \boldsymbol{U}(k) = \boldsymbol{U}(k-1)\bar{\boldsymbol{V}}(k-1) \\ \boldsymbol{D}(k) = [\bar{\boldsymbol{D}}(k-1)]^{-1} \\ \boldsymbol{P}(k) = \boldsymbol{U}(k)\boldsymbol{D}^2(k)\boldsymbol{U}^T(k) \end{cases} \tag{23}$$

Step 5: One-step parameter bias compensation calculation using Equation (24).

$$\widehat{\boldsymbol{\theta}}_{BC}(k) = \widehat{\boldsymbol{\theta}}_{LS}(k) + k\boldsymbol{\sigma}^2(k)\boldsymbol{P}(k)\boldsymbol{D}\widehat{\boldsymbol{\theta}}_{BC}(k-1) \tag{24}$$

In Equations (18) to (24), $\boldsymbol{I}$ represents the identity matrix. $\widehat{\boldsymbol{U}}(k)$and $\widehat{\boldsymbol{V}}(k)$ are $(n+1)\times(n+1)$ and $n \times n$ dimensional matrices, respectively, the left and right singular arrays of the matrix $\boldsymbol{\Sigma}$. $\boldsymbol{D}(k)$ is an $(n+1)\times n$ -dimensional diagonal array whose elements on the main diagonal are singular values of $\boldsymbol{\Sigma}$ and are non-negative. The

block diagram of its signal flow is shown in Figure 3.

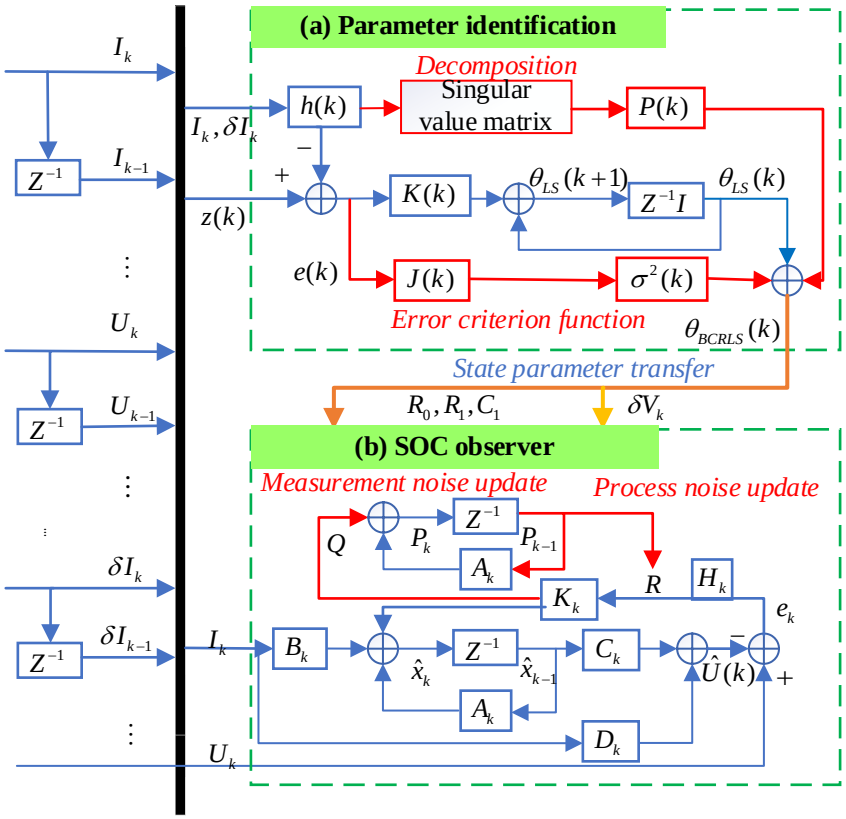

Figure 3. Schematic diagram of the proposed SVD-BCRLS-MWAEKF observer

In sub-Figure 3 (a), the input signals are $I_k, U_k, \delta I_k$, and the output signal is $\boldsymbol{\theta}_{BCRLS}$. On the one hand, when each k is added to another time step, the criterion function $\boldsymbol{J}(k-1)$ obtains the modulating factor from the error variable $\boldsymbol{e}(k)$, and the known input information $\boldsymbol{h}(k)$ and adjusts the value of the criterion function $\boldsymbol{J}(k)$ in real-time in Equation (21). Then, $\boldsymbol{\sigma}^2(k)$ as an adjustment parameter completes the update of $\boldsymbol{\theta}_{BCRLS}$, where the $\boldsymbol{D}$ is a diagonal matrix, whose diagonal elements take values that is selected for the parameters to be adjusted. On the other hand, the error covariance matrix $\boldsymbol{P}(k)$ is obtained using the decomposition of the eigenvalues to obtain its update in Equations (23), avoiding the computational complexity of solving the inverse matrix directly, accuracy and stability are achieved. Finally, the results of the parameter identification are derived using Equation (25).

$$\begin{cases} R_0 = \dfrac{\theta_2 - \theta_3}{1-\theta_1} \\ \tau = R_1 C_1 = \dfrac{1-\theta_1}{2\theta_1 + 2} \\ R_1 = (1+2\tau)\theta_2 - 2R_0\tau - R_0 \\ C_1 = \dfrac{\tau}{R_1} \end{cases} \tag{25}$$

2.4 *Moving window adaptive extended Kalman filtering method for SOC estimation*

After the model parameters of the battery are determined, the state parameter estimation also requires a precise algorithm to improve its accuracy. Using this concept, the state noise must be added to the system equation for the co-estimation, making the state-space equation suitable for the co-estimation of state noise and SOC, as shown in Equation (26).

$$\begin{cases} \widehat{\boldsymbol{x}}_{k|k-1} = \boldsymbol{A}_{k-1}\widehat{\boldsymbol{x}}_{k-1|k-1} + \boldsymbol{B}_{k-1}u_{k-1} + \boldsymbol{w}_k \\ \boldsymbol{y}_k = \boldsymbol{C}_k\widehat{\boldsymbol{x}}_{k|k-1} + \boldsymbol{D}_k u_k + \boldsymbol{v}_k \end{cases} \tag{26}$$

In Equation (26),$\boldsymbol{A}_k, \boldsymbol{B}_k, \boldsymbol{C}_k$, and $\boldsymbol{D}_k$ are the state-transition matrix, control-input matrix, observation matrix, and transfer matrix, respectively. $\boldsymbol{w}_k$ is the process noise and $\boldsymbol{v}_k$ is the observation noise at time step k. Suppose the state variable matrix is defined as $\widehat{\boldsymbol{x}}_{s,k|k-1} = [z_k\ U_{1,k}\ \delta V_k]^T, u_k = I_k$, based on Equation (9), the system equation's expressions can be constructed, as shown in Equation (27).

$$\begin{cases} \boldsymbol{A}_k = diag\left[1 \quad e^{-\frac{\Delta k}{R_{1,k-1}C_{1,k-1}}} \quad \Pi_{k,k-1}\right] \\ \boldsymbol{B}_k = \left[\dfrac{\Delta k}{C_{cap}} \quad R_{1,k-1}\left(1 - e^{-\frac{\Delta k}{R_{1,k-1}C_{1,k-1}}}\right) \quad 0\right]^T \\ \boldsymbol{C}_k = [C_{1,k} \quad 1 \quad 1]^T \\ \boldsymbol{D}_k = [-R_0] \\ \boldsymbol{w}_k = \left[\dfrac{\Delta k}{C_{cap}}\delta I_k \quad 0 \quad \delta I_k\right]^T \end{cases} \tag{27}$$

As shown in Equation (27), the process noise $\boldsymbol{w}_k$ has similar properties to current fluctuations δI_k and varies with the noise characteristics of the current. In addition, $C_{1,k}$ is the result of linearization from the nonlinear fitting $U_{oc,k}(z_k)$, as shown in Equation (28).

$$U_{oc,k} \approx z_k \cdot \frac{d(U_{oc}(k))}{d(SOC(k))}\Big|_{z_k = SOC(k)} = z_k \cdot C_{1,k} \tag{28}$$

Based on the effect of process noise, the MWAEKF algorithm is proposed to estimate the SOC of the lithium-ion battery. The main iterative equations based on MWAEKF are as follows:

Initialization at time step $k = 0$:

Step 1: Initialization of identified parameter $\widehat{\boldsymbol{x}}_0$ and error covariance matrix $\boldsymbol{P}_0$, as shown in Equation (29).

$$\begin{cases} \widehat{\boldsymbol{x}}_0 = E[\boldsymbol{x}_0] \\ \boldsymbol{P}_0 = E[(\boldsymbol{x}_0 - \widehat{\boldsymbol{x}}_0)(\boldsymbol{x}_0 - \widehat{\boldsymbol{x}}_0)^T] \end{cases} \tag{29}$$

At the time step $k = 1,2, \ldots, N$, repeat:

Step 2: One-step calculation of the state $\hat{\boldsymbol{x}}_{k|k-1}$ and error covariance matrix $\boldsymbol{P}_{k|k-1}$ using Equation (30).

$$\begin{cases} \hat{\boldsymbol{x}}_{k|k-1} = \boldsymbol{A}_{k-1}\hat{\boldsymbol{x}}_{k-1|k-1} + \boldsymbol{B}_{k-1}u_{k-1} + \boldsymbol{R}_{k-1} \\ \boldsymbol{P}_{k|k-1} = \boldsymbol{A}_{k-1}\boldsymbol{P}_{k-1|k-1}\boldsymbol{A}_{k-1}^{T} + \boldsymbol{Q}_{k-1} \end{cases} \tag{30}$$

Step 3: One-step update of the state estimate $\hat{\boldsymbol{x}}_k$ and error covariance matrix $\boldsymbol{P}_k$, as shown in Equation (31).

$$\begin{cases} \boldsymbol{K}_k = \boldsymbol{P}_{k|k-1}\boldsymbol{C}_k^{T}(\boldsymbol{C}_k\boldsymbol{P}_{k|k-1}\boldsymbol{C}_k^{T} + \boldsymbol{R}_{k-1})^{-1} \\ \boldsymbol{e}_k = \boldsymbol{y}_k - (\boldsymbol{C}_k\hat{\boldsymbol{x}}_{k|k-1} + \boldsymbol{D}u_k) \\ \hat{\boldsymbol{x}}_k = \hat{\boldsymbol{x}}_{k|k-1} + \boldsymbol{K}_k\boldsymbol{e}_k \\ \boldsymbol{P}_k = \boldsymbol{P}_{k|k-1} - \boldsymbol{K}_k\boldsymbol{C}_k\boldsymbol{P}_{k|k-1} \end{cases} \tag{31}$$

Step 4: One-step update of the variance of the process noise and observation noise, as shown in Equations (32) and (33).

$$\boldsymbol{H}_k = \begin{cases} \dfrac{k-1}{k}\boldsymbol{H}_{k-1} + \dfrac{1}{k}\boldsymbol{e}_k{\boldsymbol{e}_k}^{T}, k \le W \\ \dfrac{1}{W}\displaystyle\sum_{i=k-W+1}^{k}\boldsymbol{e}_i{\boldsymbol{e}_i}^{T}, k > W \end{cases} \tag{32}$$

$$\begin{cases} \boldsymbol{Q}_k = \boldsymbol{K}_k\boldsymbol{H}_k{\boldsymbol{K}_k}^{T} \\ \boldsymbol{R}_k = \boldsymbol{H}_k - \boldsymbol{C}_k\boldsymbol{P}_{k|k-1}{\boldsymbol{C}_k}^{T} \end{cases} \tag{33}$$

In Equations (32) and (33), the W is the size of the moving window, and the $\boldsymbol{H}_k$ is the variance of the algorithmic errors. The process noise covariance $\boldsymbol{Q}_k$ and observation noise covariance $\boldsymbol{R}_k$ are the results of adaptive filtering algorithms based on moving windows, which can dynamically adjust the variance size of the algorithmic errors by changing the length of window W. As is shown in Figure 3 (b), the suitable window function $\boldsymbol{H}_k$ is calculated through the error $\boldsymbol{e}_k$, and the adequate amount of $\boldsymbol{Q}_k$ is obtained through the evaluation of the $\boldsymbol{H}_k$ and $\boldsymbol{K}_k$. On the other hand, the update for $\boldsymbol{R}_k$ is obtained using the joint action of covariances $\boldsymbol{P}_{k|k-1}$ and $\boldsymbol{H}_k$, which corrects the result of the Kalman gain $\boldsymbol{K}_k$. Finally, the updated results for the state quantity are corrected. The overall flowchart of the SVD-BCRLS-MWAEKF estimation-based algorithm is shown in Figure 4.

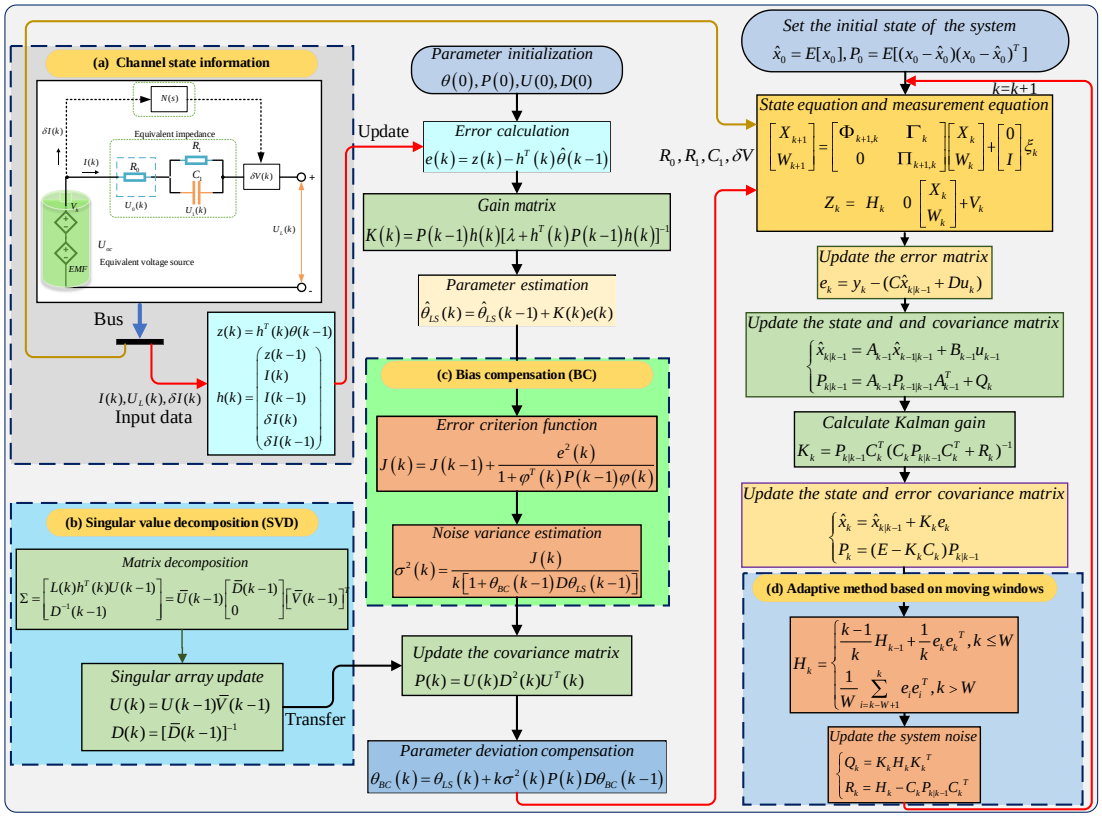

Figure 4. The flowchart of the SVD-BCRLS-MWAEKF algorithm

In Figure 4, Section (a) is the result of the channel information measured from NBC-ECM. The data information is obtained from the model and input into the algorithm for online parameter identification. The parameters are accurately identified under the combined effect of Section (b), the calculation for the NBC, and Section (c), the calculation of the $\boldsymbol{P}_{k|k-1}$ matrix by eigenvalue decomposition. Section (d) is the adaptive method based on the moving window approach. The acquired parameter and data information are imported into the NBC-ECM framework to update and obtain the system noise and measurement noise using the improved adaptive window function.

2.5. *Performance evaluation metrics*

Three standard evaluation metrics are employed to verify the performance of the proposed methods, which include the maximum error (MAX), root mean square error (RMSE), and mean absolute error (MAE). Their mathematical calculations are expressed in Equation (34).

$$\begin{cases} E_k = y_k - \hat{y}_k \\ RMSE = \sqrt{\dfrac{1}{N}\sum_{k=1}^{N}(y_k - \hat{y}_k)^2} \\ MAE = \dfrac{1}{N}\sum_{k=1}^{N}|y_k - \hat{y}_k| \\ MAX = max|y_k - \hat{y}_k|; 1 \le k \le N \end{cases} \tag{34}$$

As shown in Equation (34), E_k is the difference between the actual value y_k and estimated value $\hat{y}_k$. The RMSE is used to measure the deviation between the actual value y_k and estimated value $\hat{y}_k$. The MAE indicates that in the error data sequence, all individual differences between positive and negative data values are equally weighted. These two equations explain the evaluation metrics from different angles. If the dispersion of the estimated error is high, the RMSE will increase more than the MAE. The MAX represents the absolute maximum error in the estimated error data sequence.

3. Results and discussion

3.1. *Battery tests and data collection*

To verify the performance of the proposed SVD-BCRLS-MWAEKF estimation-based algorithm based on the proposed NBC-ECM, battery tests under different operating conditions are conducted using a commercial ternary lithium battery (LNMC70 Ah) as the research object. The established experimental test platform and specifications of the test battery are shown in Figure 5.

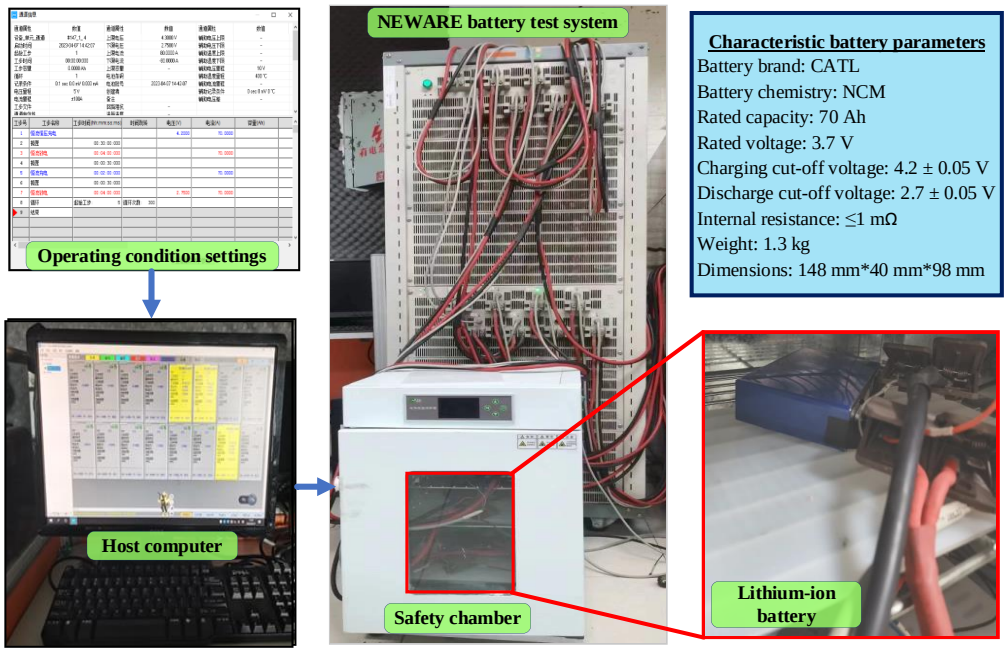

Figure 5. Experimental test platform and battery parameters

As shown in Figure 5, a NEWARE battery charge and discharge test system (CT-4016-5V100A) is used for the experiment under different operating conditions. Before the test, step settings using the host computer and real-time data can be obtained via the TCP/IP network cable. For each test condition, the lithium-ion battery is placed in a chamber at a constant temperature to ensure the safety of the battery during its operation. Then, the host computer is used to program the working steps for the charge and discharge tester to complete the battery test under each operating condition. Table 1 displays the technical specifications of the NEWARE battery charge and discharge test system.

Table 1. Specifications of the NEWARE battery test system

Property	Parameter
Working current range	0.5~100 A
Voltage range	0.025–5 V
Output power	14.2 kW
Available test channels	16
Measurement accuracy	±0.1% full-scale rating
Data acquisition interval	0.1 s

This study adopts the HPPC and BBDST datasets obtained at a room temperature of about 25 ℃. Three capacity tests are conducted to obtain the actual capacity of the battery, which is 68.47 Ah. The constant current-constant voltage (CC-CV) charging method promotes longer battery life and increased safety by switching between CC charging, which prevents overcurrent, and CV charging, which avoids overvoltage, based on the battery's state. All the operating condition tests begin with a CC-CV charging method, which is applied until the maximum capacity of the battery is attained. The discharge steps are applied after a 40-minute rest to ensure thermal and electrochemical equilibrium. More details about the typical HPPC and BBDST experimental procedures can be obtained in [11, 21]. The characteristic voltage and current datasets obtained from the HPPC and BBDST experiments are shown in Figure 6.

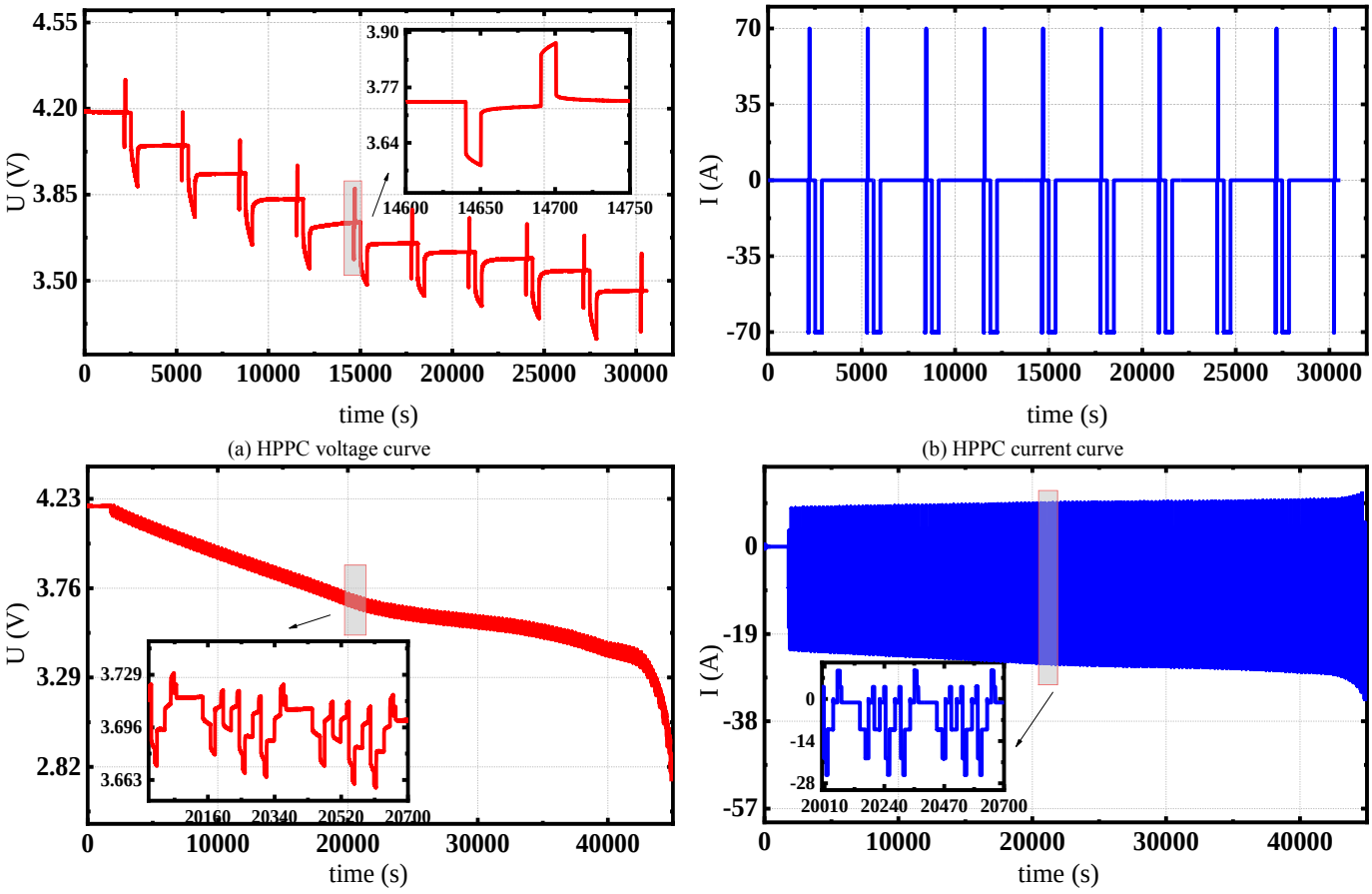

(a) HPPC voltage curve

(b) HPPC current curve

(c) BBDST voltage curve

(d) BBDST current curve

Figure 6. The characteristic voltage and current curves under different operating conditions

3.2. *Validation of terminal voltage tracking effect based on the NBC-ECM*

Firstly, current, voltage, and current fluctuation noise as input are involved in the identification of the noise model. For the test environment, the NEWARE battery charge and discharge test system have a test accuracy of ±0.1% full scale. However, to reflect the effectiveness of the algorithm and fully reflect the bias correction characteristics of the noise model in the electromagnetic environment, the input current fluctuation is set to 0.01A. Then, to analyze the adaptability of the NBC-ECM, the estimation effects of Gaussian observation noise $\boldsymbol{R} = 0$ V/A, $\boldsymbol{R} = 0.01$ V/A, $\boldsymbol{R} = 0.05$ V/A, and colored process noise $\boldsymbol{Q}$ are discussed. The data with Gaussian white noise is entered into the model as contaminated data. The colored process noise $\boldsymbol{Q}$ is 100 times δV_k calculated based on the Equation (15) using the NBC-ECM and $\delta I_k = 0.01$ V/A. Given that the battery is a nonlinear system with noise interference, the impact of noise on battery parameters and SOC estimation accuracy is investigated using parameter identification and SOC estimation algorithms for further verification under various operating conditions. For the parameter identification algorithms, the RLS, BCRLS, and SVD-BCRLS are used to identify the parameters of the battery based

on input current and voltage with and without noise. Moreover, based on the performance of the proposed SVD-BCRLS algorithm, its parameters are used as input to test and verify the performance of the proposed MWAEKF SOC estimation algorithm under various noise and operating conditions. Then, the estimations of the proposed MWAEKF algorithm are compared to the EKF and AEKF algorithms for further verification.

3.2.1 Adaptation of the battery model to different operating conditions

The comparative results of the monitored and simulated voltages by the established battery NBC-ECM using different parameter identification algorithms and conducted with different noise interferences under the HPPC operating condition. Using the proposed SVD-BCRLS algorithm, the voltage traction characteristics are carried out considering different measurement noise and compared with the RLS and BCRLS algorithms to verify its performance, as shown in Figure 7.

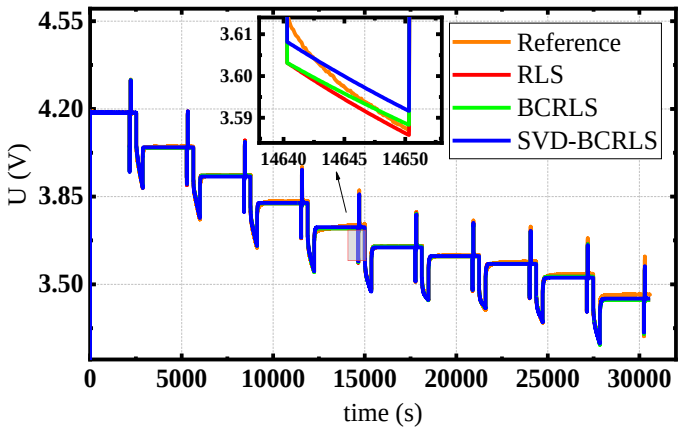

(a-1) Comparative voltage traction results

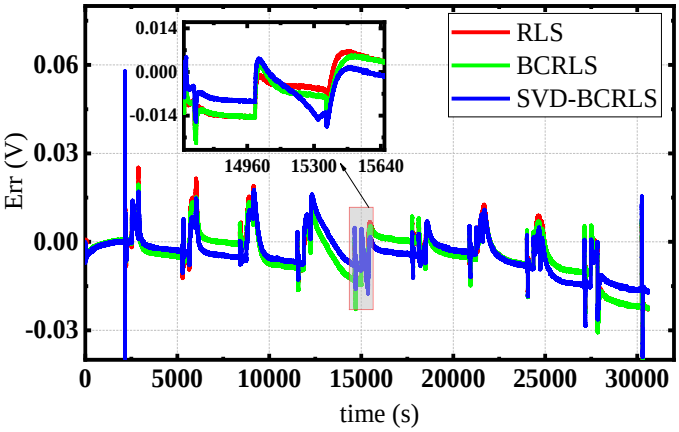

(a-2) Comparative voltage error results

(a) Gaussian observation noise $\boldsymbol{R} = 0$ V/A

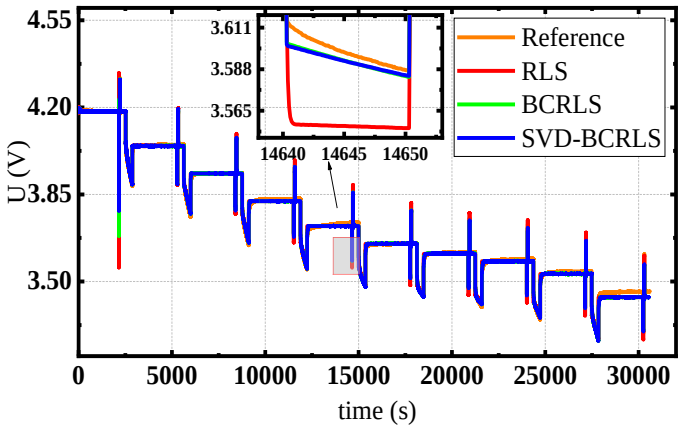

(b-1) Comparative voltage traction results

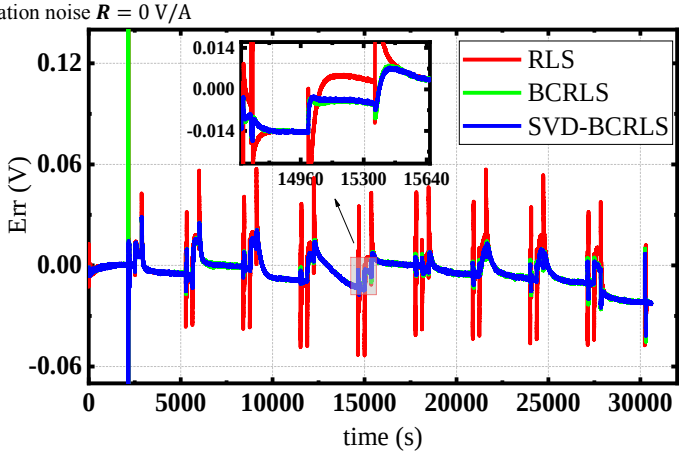

(b-2) Comparative voltage error results

(b) Gaussian observation noise $\boldsymbol{R} = 0.01$ V/A

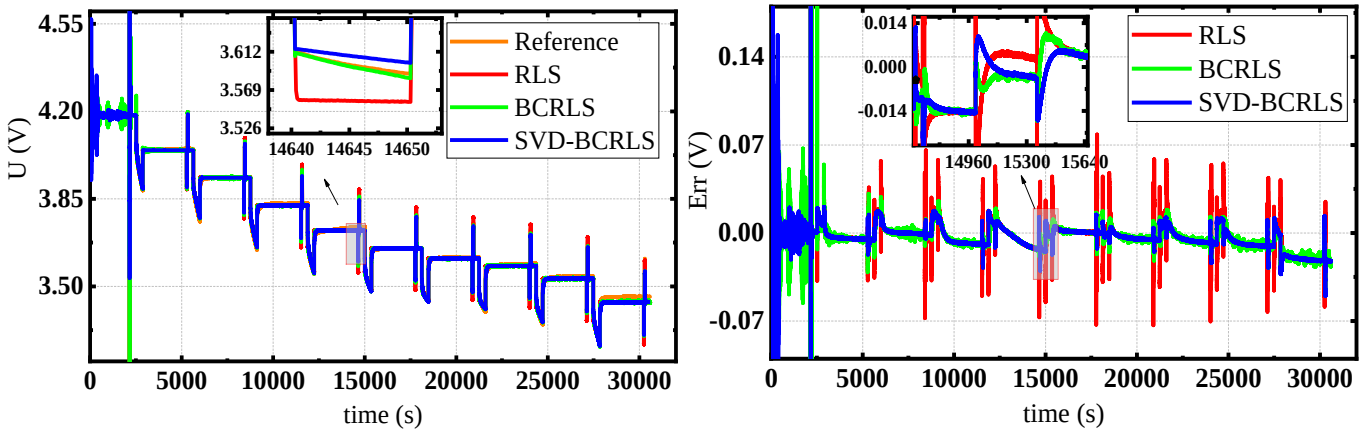

(c-1) Comparative voltage traction results

(c-2) Comparative voltage error results

(c) Gaussian observation noise $\boldsymbol{R} = 0.05$ V/A

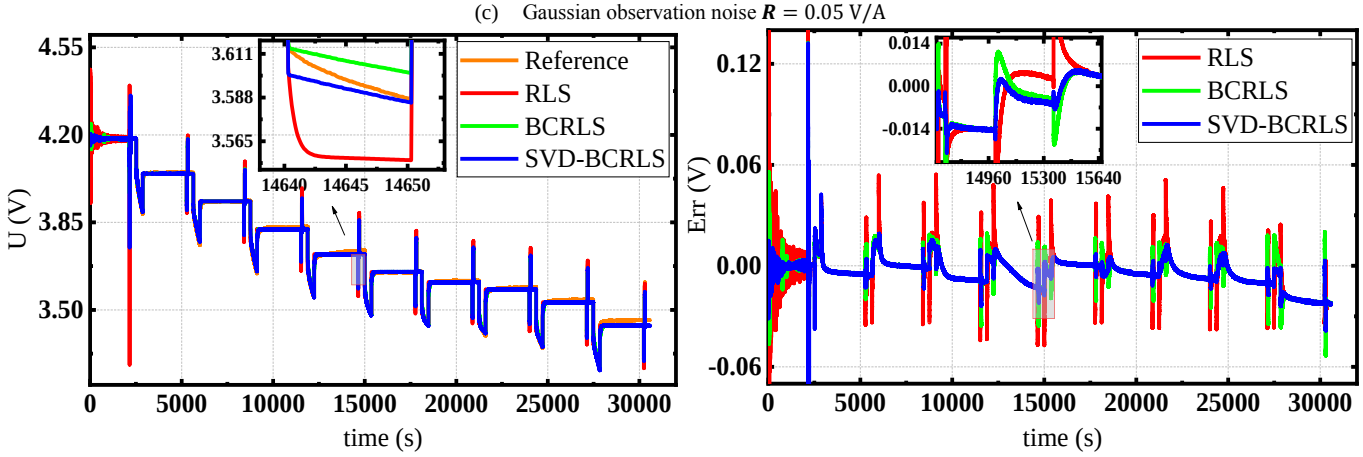

(d-1) Comparative voltage traction results

(d-2) Comparative voltage error results

(d) Colored noise $\boldsymbol{Q}$

Figure 7. Voltage tracking results for different identification algorithms under the HPPC operating condition

As shown in Figure 7 (a), without any noise, it can be observed that the voltage traction results using the SVD-BCRLS algorithm have better performance compared to the RLS and BCRLS algorithms under the HPPC operating condition. From the results, it can be observed that the proposed SVD-BCRLS algorithm can correct the initial noise fluctuations that affect the other algorithms, especially when noise values of 0.01 and 0.05 V/A are used. Compared to the BCRLS algorithm, the SVD-BCRLS has a very stable drop at each discharge period and around the zero value from 2500 s to the end of discharge, as shown in Figure 7 (a-2). An obvious change begins when a noise value of 0.01 V/A is applied, as shown in Subfigure 7 (b). Based on the voltage traction results, it can be observed that the RLS and BCRLS algorithms have constant errors in the process of discharge time, whereas the SVD-BCRLS shows good convergence and low noise effects. Also, as the measurement noise value $\boldsymbol{R} = 0.05$ V/A increases, the error superimposed on the input data increases the voltage errors using the BCRLS algorithm, as shown in Figure 7 (c). However, the voltage error still has good stability using the SVD-BCRLS algorithm. The most obvious change appears in Figure 7(d) when the system color noise is applied. The BCRLS displays fewer voltage estimation results

during battery discharge, but the SVD-BCRLS has good adaptability, showing a more robust result until the end of discharge.

To further verify the performance of the proposed SVD-BCRLS parameter identification algorithm, the MAE and RMSE metrics are employed, as shown in Table 2.

Table 2. Comparative results of the voltage errors using different noise characteristics

Noise interference	Metric	RLS	BCRLS	SVD-BCRLS
$\boldsymbol{R} = 0\mathrm{V/A}$	RMSE	0.8627%	0.7809%	0.7717%
	MAE	0.6321%	0.6234%	0.6092%
$\boldsymbol{R} = 0.01\ \mathrm{V/A}$	RMSE	1.014%	0.8712%	0.8684%
	MAE	0.7298%	0.6384%	0.6363%
$\boldsymbol{R} = 0.05\ \mathrm{V/A}$	RMSE	1.036%	1.665%	1.008%
	MAE	0.7353%	0.6955%	0.6944%
$\boldsymbol{Q}$	RMSE	1.071%	0.9148%	0.8772%
	MAE	0.7569%	0. 6690%	0.6379%

From Table 2, using $\boldsymbol{R} = 0.0\ \mathrm{V/A}$, it can be observed that the RMSE and MAE values of the proposed SVD-BCRLS algorithm are 0.7717% and 0.6092%, which shows that the proposed algorithm has improved accuracy compared to the RLS and BCRLS algorithms. Furthermore, using different noise values of 0.01 and 0.05 V/A, it can be shown that the proposed SVD-BCRLS algorithm has optimal voltage tracking capability by showing RMSE and MAE values of 0.8684% and 1.008%, and 0.6363% and 0.6944%, respectively, which are less than those of the RLS and BCRLS parameter identification algorithms.

To further verify the performance of the proposed SVD-BCRLS algorithm in comparison to the RLS and BCRLS, the battery verification is carried out using different noise values under the complex BBDST operating condition, as shown in Figure 8.

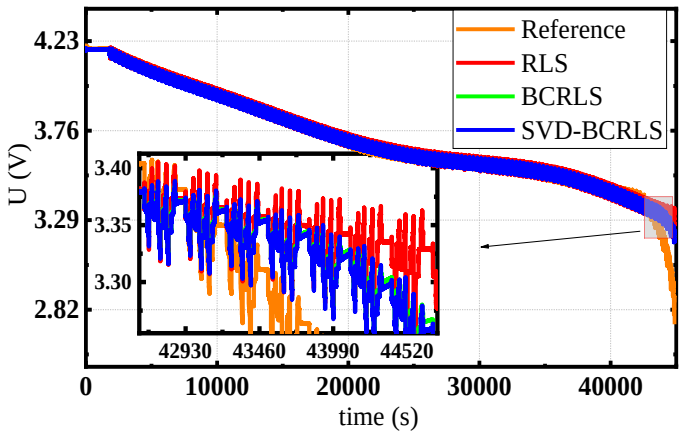

(a-1) Comparative voltage traction results

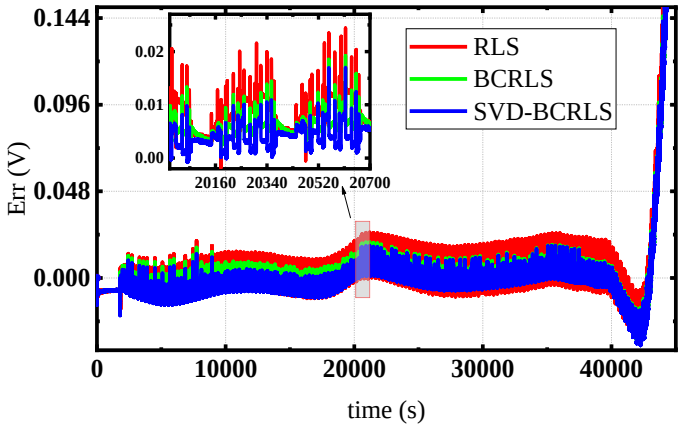

(a-2) Comparative voltage error results

(a) Gaussian observation noise $\boldsymbol{R} = 0$ V/A

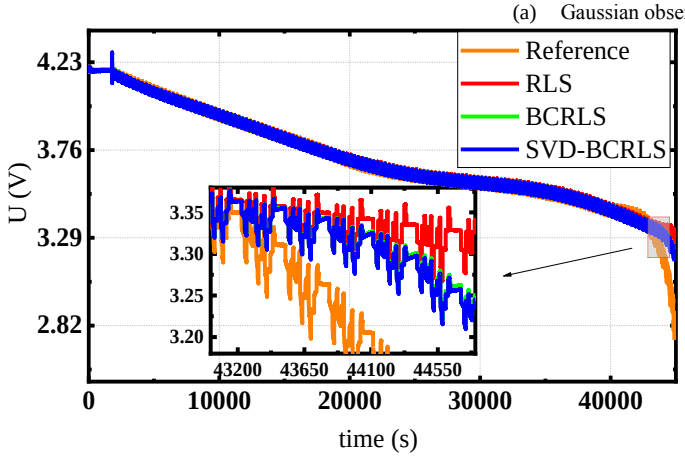

(b-1) Comparative voltage traction results

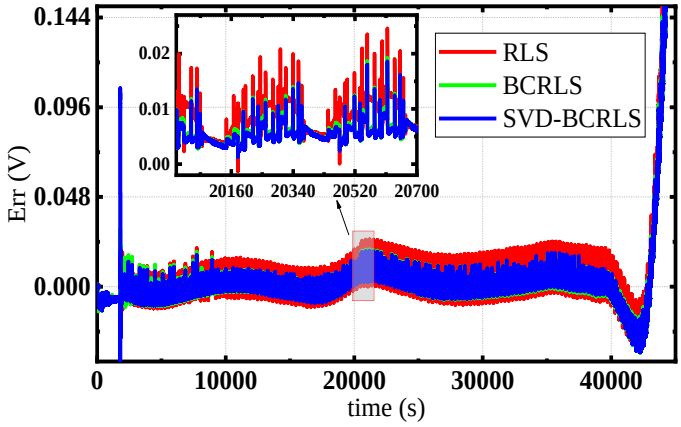

(b-2) Comparative voltage error results

(b) Gaussian observation noise $\boldsymbol{R} = 0.01$ V/A

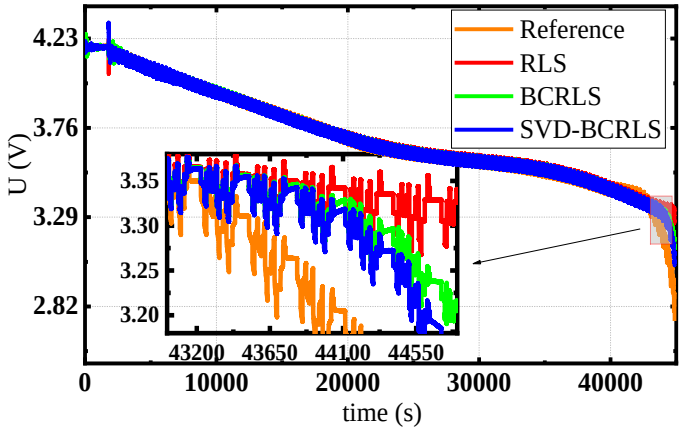

(c-1) Comparative voltage traction results

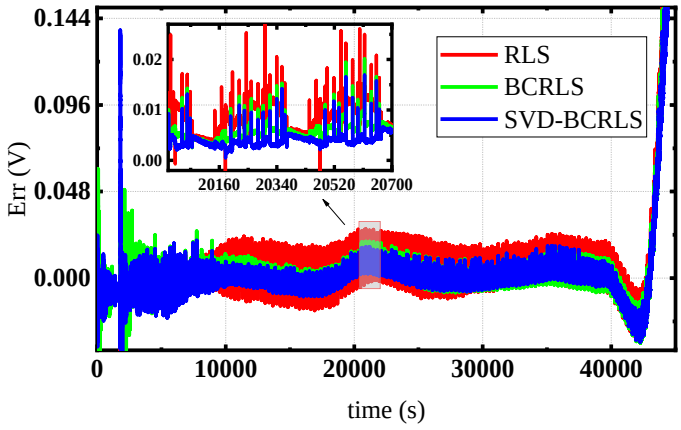

(c-2) Comparative voltage error results

(c) Gaussian observation noise $\boldsymbol{R} = 0.05$ V/A

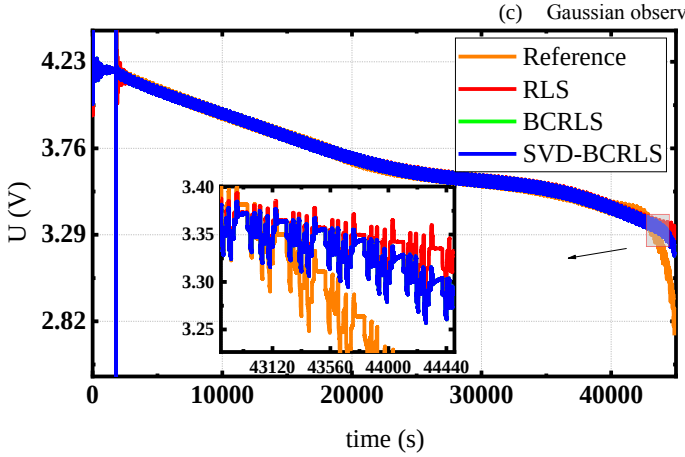

(d-1) Comparative voltage traction results

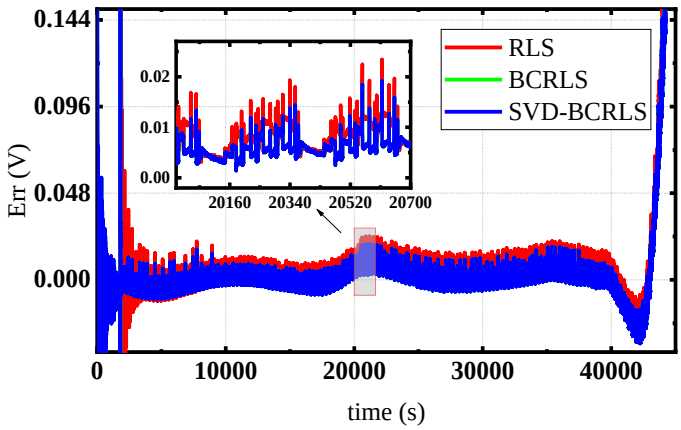

(d-2) Comparative voltage error results

(d) Colored noise $\boldsymbol{Q}$

Figure 8. Voltage tracking results for different identification algorithms under the BBDST operating condition

As shown in Figure 8 (a-1), without noise, it can be observed that the SVD-BCRLS algorithm performs a good convergence role in treating battery discharge time. The bias compensation effect in the RLS is more clearly demonstrated at the end of discharge, which shows a steep decline caused by the characteristics of the battery at low SOC levels. According to the estimation result for noise $\boldsymbol{R} = 0.05\ \mathrm{V/A}$, the objective of the SVD optimization occurs when the noise amplitude is large, or when the battery discharge deviation is large, as shown in Figure 8 (c). Also, at a low SOC level, it can be observed that the SVD-BCRLS optimization effect is also better than that of the BCRLS algorithm. At the same time, it can be observed that the voltage error of the SVD-BCRLS algorithm has an error drop at the time of 1000–2000 s compared with the BCRLS algorithm, which is due to the SVD's ability to accelerate the convergence rate. When an input noise is colored noise $\boldsymbol{Q}$, the estimated results of voltage for the BCRLS and SVD-BCRLS algorithms are both better than the RLS algorithm. One possible reason is that the colored noise is extracted from the NBC-ECM, which is an extension of the Thevenin ECM. Therefore, the colored noise has the characteristics of that compensation model when the bias compensation is effective. The RLS algorithm cannot finish the error correction with bias compensation. But both the BCRLS and SVD-BCRLS algorithms can change the spectrum structure of colored noise and have the same voltage tracking result.

A more thorough comparison of the proposed identification algorithm is presented in Table 3, along with the RLS and BCRLS algorithms' results under the BBDST operating condition.

Table 3 Comparative results of the voltage errors using different noise characteristics

Noise interference	Metric	RLS	BCRLS	SVD-BCRLS
$\boldsymbol{R} = 0\ \mathrm{V/A}$	RMSE	4.035%	3.381%	3.300%
	MAE	1.154%	0.972%	1.035%
$\boldsymbol{R} = 0.01\ \mathrm{V/A}$	RMSE	4.009%	3.299%	3.243%
	MAE	1.145%	0.9550%	0.9473%
$\boldsymbol{R} = 0.05\ \mathrm{V/A}$	RMSE	4.010%	3.117%	2.656%
	MAE	1.145%	0.9550%	0.9473%
$\boldsymbol{Q}$	RMSE	4.033%	5.017%	5.017%
	MAE	1.151%	1.032%	1.032%

From Table 3, it can be observed that using the SVD-BCRLS algorithm, the RMSE is 3.300% compared to

3.381% for the BCRLS algorithm, which is better than the RLS algorithm's value of 4.035%, showing the optimal adaptability to the voltage of the battery under the BBDST operating condition. At a noise value of 0.01 V/A, it can be observed that the SVD-BCRLS algorithm is slightly optimized. The RMSE of the SVD-BCRLS algorithm is 3.243%, which is also better than 3.299% for the BCRLS algorithm. Furthermore, the comparative results show that when the noise amplitude is $\boldsymbol{R} = 0.05$ V/A, the RMSE for the SVD-BCRLS is 2.656%, which is better than the BCRLS and RLS, which have RMSEs of 3.117% and 4.010%, respectively. From the longitudinal comparison, the RMSE decreased by 0.027% when the noise amplitude increased from 0 to 0.01 V/A and by 0.587% when the noise amplitude increased from 0.01 to 0.05 V/A, which means when the noise amplitude increased by five times from 0 to 0.05 V/A, the RMSE decreased by 0.614%. These results prove that the optimization characteristic of the SVD-BCRLS algorithm is more suitable for parameter identification under the influence of electromagnetic noise.

3.2.2 Parameters identification of the SVD-BCRLS algorithm

An accurate ECM is the most significant factor in preventing battery model voltage and SOC divergence and ensuring the safety of the EV. Following model validation, the performance of the proposed SVD-BCRLS algorithm in identifying battery parameters is tested and compared to that of the RLS and BCRLS algorithms to validate its performance. Using the RLS, BCRLS, and SVD-BCRLS parameter identification algorithms, the R_0, R_1, C_1, and δV_k with a noise value of $\boldsymbol{R} = 0.01$ V/A are identified under the HPPC operating condition, as shown in Figure 9.

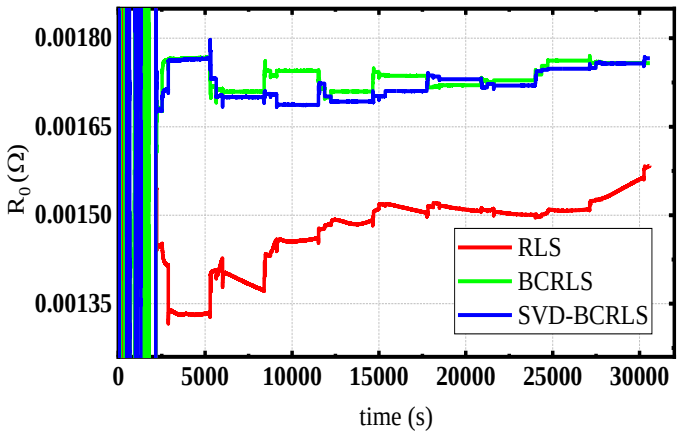

(a) Internal ohmic resistance: R_0

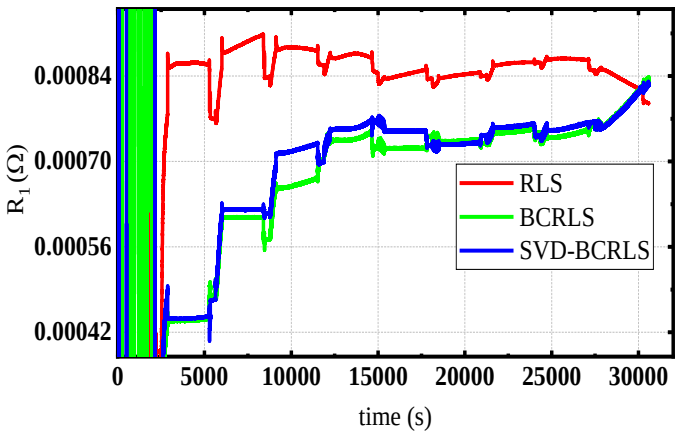

(b) Electrochemical polarization resistance: R_1

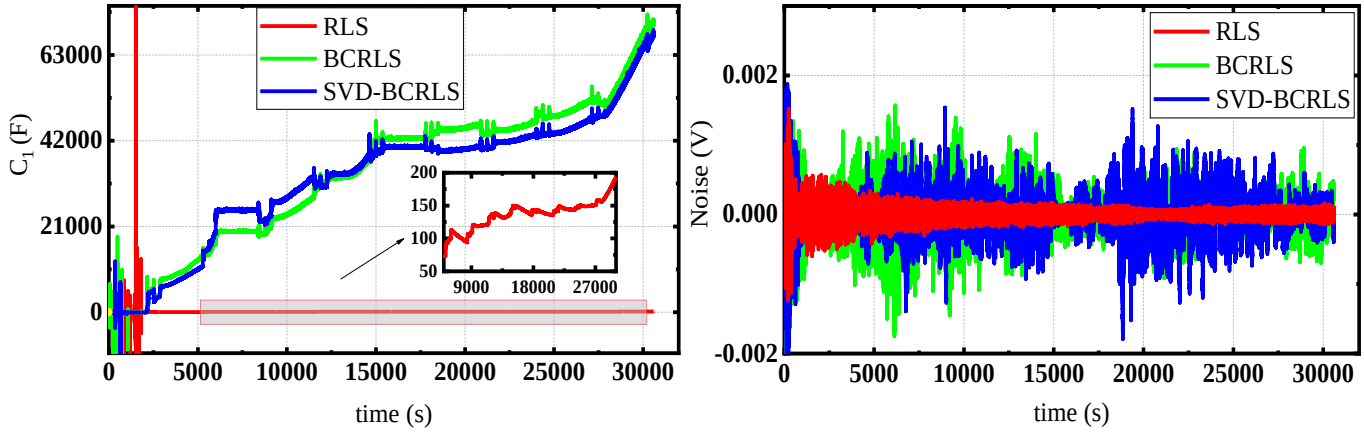

(c) Electrochemical polarization capacitance: C_1 (d) Noise voltage: δV_k

Figure 9. Identification of battery parameters using different algorithms

In Figure 9 (a), comparing the increased trend of the RLS and the larger fluctuation of the BCRLS algorithm, the SVD-BCRLS has a more stable trend. In Figure 9 (b) and (c), the changing trends of the BCRLS and SVD-BCRLS algorithms for the R_1 and C_1 tend to be monotonically increasing during discharge time. It is because the BC method can overcome the noise uncertainties and makes the dynamic characteristics more adequate, which are visible in the resistance and capacitance changes. Comparing the results obtained for the R_1 and C_1, it can be observed that both the BCRLS and SVD-BCRLS algorithms show a similar increasing trend. However, the results of the BCRLS have noisy changes, which makes the SVD-BCRLS a more suitable algorithm for identifying the parameters of the battery. On the other hand, the R_1 estimation by the RLS shows an increasing trend, which remains constant until the end of discharge, where it begins to show a downward trend, which means it loses robustness in identifying the parameter of the battery until a full discharge state. Also, the RLS is observed to have a very small C_1, which means it cannot sufficiently identify the parameter of the battery. As shown in Figure 9 (d), the noise values of the BCRLS and SVD-BCRLS algorithms have a higher ability to identify the noise component from the middle to the end of discharge than the RLS algorithm, which shows the RLS cannot identify the noise and it can be extracted using the BC. Moreover, the role of the SVD has been reflected in the stability of mid-discharge time, demonstrating the optimal characterization of the SVD for the stability of parameter identification.

3.3. *SOC estimation based on the SVD-BCRLS-MWAEKF algorithm*

This section presents the SOC estimation results using different noise interference for $\boldsymbol{Q}_k$ and $\boldsymbol{R}_k$ to update the noise under the HPPC and BBDST operating conditions. After verifying that the established battery model provides

a reliable representation of the battery, the identified parameters of the SVD-BCRLS algorithm are then utilized for estimating the SOC based on the proposed MWAEKF algorithm. To further verify the performance of the proposed SOC estimation algorithm, the EKF and Saga-Husa-based EKF (AEKF) algorithms are also employed.

3.3.1 Impact of noise on the SOC under the HPPC operating condition

The comparative estimation results using different noise interferences of the EKF, AEKF, and MWAEKF algorithms under the HPPC operating condition are shown in Figure 10.

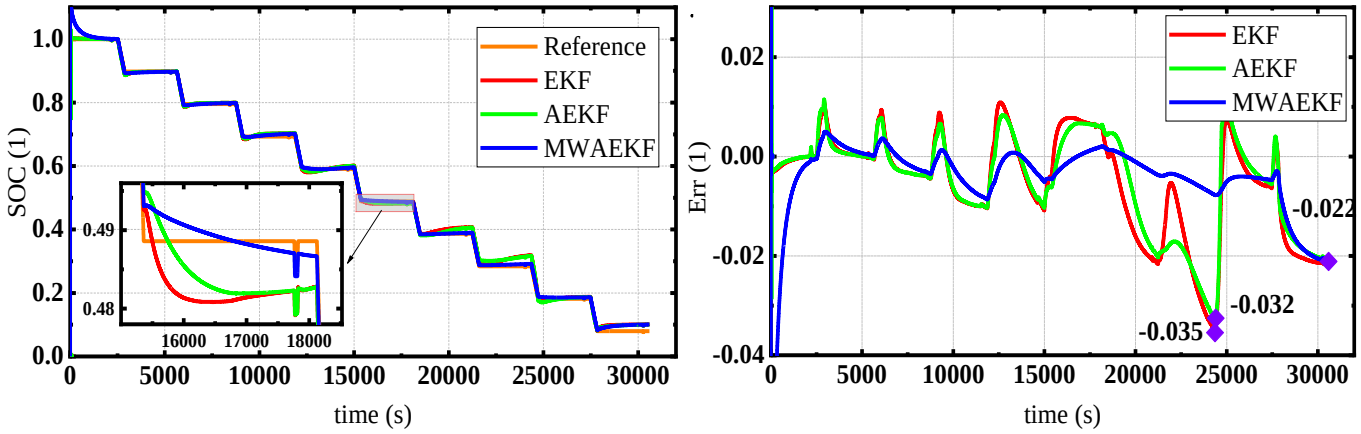

(a-1) Comparative SOC traction results (a-2) Comparative SOC error results

(a) Gaussian observation noise $\boldsymbol{R} = 0$ V/A

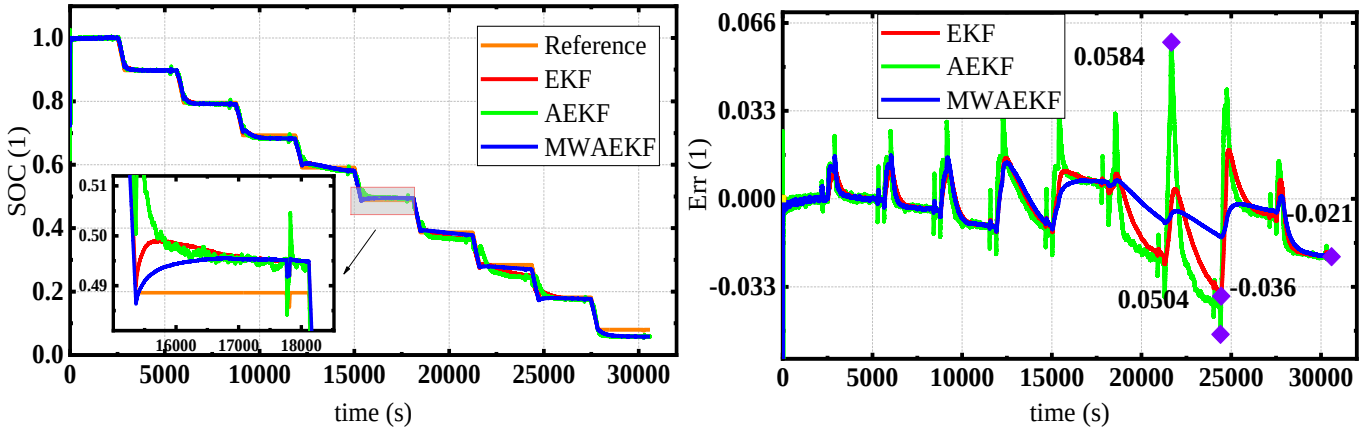

(b-1) Comparative SOC traction results (b-2) Comparative SOC error results

(b) Gaussian observation noise $\boldsymbol{R} = 0.01$ V/A

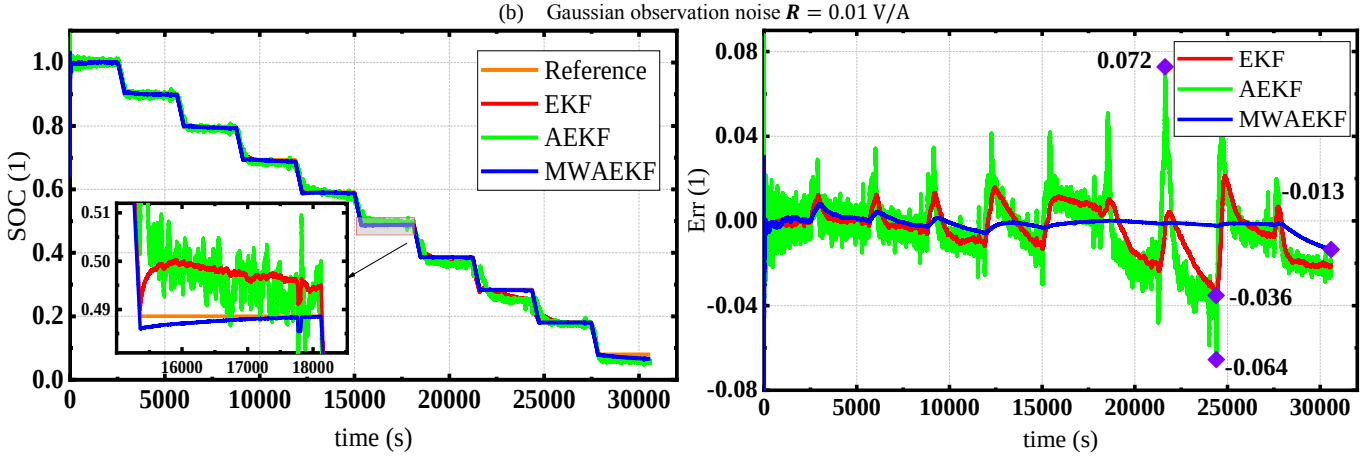

(c-1) Comparative SOC traction results (c-2) Comparative SOC error results

(c) Gaussian observation noise $\boldsymbol{R} = 0.05$ V/A

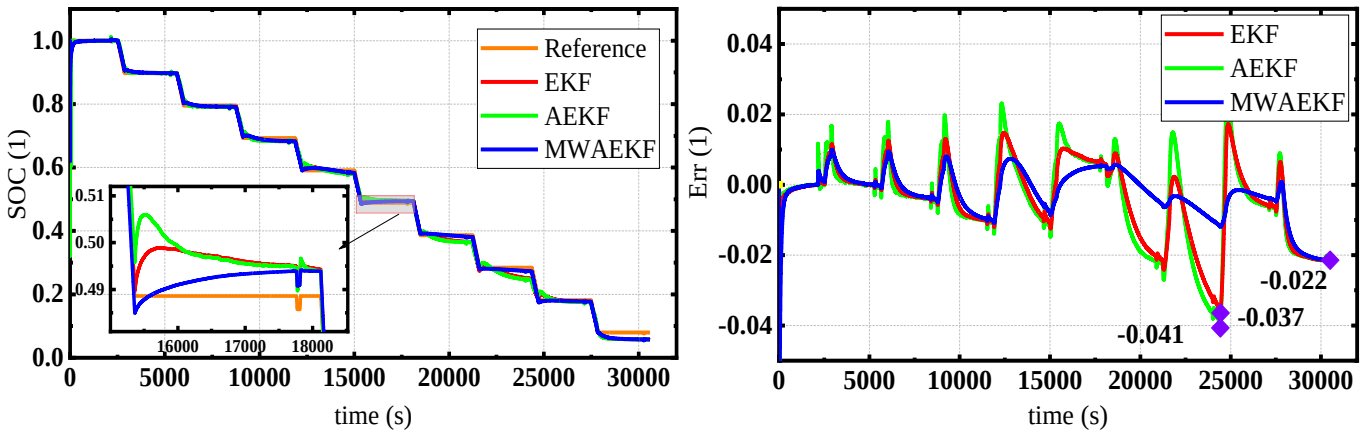

(d-1) Comparative SOC traction results (d-2) Comparative SOC error results

(d) Colored noise $\boldsymbol{Q}$

Figure 10. Comparative SOC results using different noise interferences under the HPPC operating condition

As shown in Figure 10 (a-1), the SOC estimation is carried out without a noise value. For the MWAEKF algorithm, except for the large error at the initial moment, the result of the SOC estimation quickly converges to the actual value during the whole discharge process, with a MAX of 2.2%. Meanwhile, the results of the EKF and AEKF algorithms show that they have a good convergence rate. However, their estimations tend to fluctuate much more than the MWAEKF, which results in MAXs of 3.5% for the EKF and 3.2% for the AEKF algorithm. Furthermore, when the noise value is increased to 0.01 V/A, the SOC error for the MWAEKF algorithm converges with the least MAX of 2.1%, while the EKF and AEKF have 3.6% and 5.04%, respectively. Moreover, when the noise is 0.05 V/A, the SOC error for the MWAEKF algorithm proves to be the least, showing a MAX of 1.3%. The results reflect that the proposed MWAEKF algorithm not only maintains good accuracy in the presence of different noise values but also has optimal estimation results as the noise amplitude increases. These changes demonstrate that the optimization effect improves when the noise amplitude increases from 0.01 to 0.05 V/A. Meanwhile, compared with the EKF, the AEKF algorithm has poor adaptability to the SOC estimation accuracy of different noise amplitudes. The maximum SOC error increases from 3.5% to 7.2% as the noise interference increases from 0 to 0.05 V/A. It can be observed that when the noise amplitude of the AEKF increases, not only the estimation error becomes larger, but also the convergence line becomes worse. When the colored noise $\boldsymbol{Q}$ is input into the system, the same results also confirm the improved accuracy of SOC estimation using the proposed MWAEKF algorithm, which has a MAX of 2.2%.

To further verify the SOC performance of the proposed MWAEKF algorithm, the standard metrics are employed, which are conducted and presented in comparison with the EKF and AEKF algorithms, as shown in Table 4.

Table 4. Performance evaluation results for different SOC algorithms under the HPPC operating condition

Noise interference	Metric	EKF	AEKF	MWAEKF
$\boldsymbol{R} = 0\ V/A$	RMSE	1.159%	1.101%	1.106%
	MAE	0.8411%	0.7956%	0.5427%
$\boldsymbol{R} = 0.01\ V/A$	RMSE	1.163%	1.550%	0.8387%
	MAE	0.8617%	1.130%	0.6384%
$\boldsymbol{R} = 0.05\ V/A$	RMSE	1.132%	1.604%	0.3972%
	MAE	0.8506%	1.200%	0.2316%
$\boldsymbol{Q}$	RMSE	1.165%	1.367%	0.8399%
	MAE	0.8641%	0.9889%	0.5514%

According to the performance evaluation results shown in Table 4, with no noise applied, the RMSE values of the EKF, AEKF, and MWAEKF algorithms are 1.159%, 1.101%, and 1.106%, respectively. Furthermore, the MAEs for the EKF, AEKF, and MWAEKF algorithms are 0.8411%, 0.7956%, and 0.5427%, respectively, indicating that the proposed MWAEKF outperforms the EKF and AEKF algorithms. Furthermore, using 0.01 V/A observation noise, the results show that the MWAEKF algorithm significantly improved SOC performance, with RMSE and MAE of 0.8387% and 0.6384%, respectively, which is better than the EKF (1.163% and 0.8617%) and AEKF (1.550% and 1.130%). Also, when the noise is 0.05 V/A, the RMSE and MAE of the EKF and AEKF algorithms are higher than those of the MWAEKF algorithm, and a similar pattern is observed when colored noise is used. This further illustrates the MWAEKF algorithm's excellent estimation ability and anti-interference ability in the presence of noise.

3.3.2 Impact of noise on the SOC under the BBDST operating condition

Following the completion of the battery operating tests, the actual operating conditions should be fully considered to verify the SOC estimation performance of the proposed MWAEKF algorithm. The SOC is carried out at various noise interference levels under the BBDST operating condition, as shown in Figure 11.

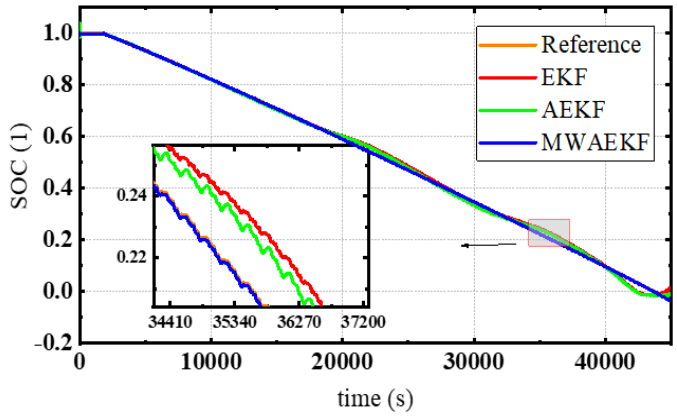

(a-1) Comparative SOC traction results

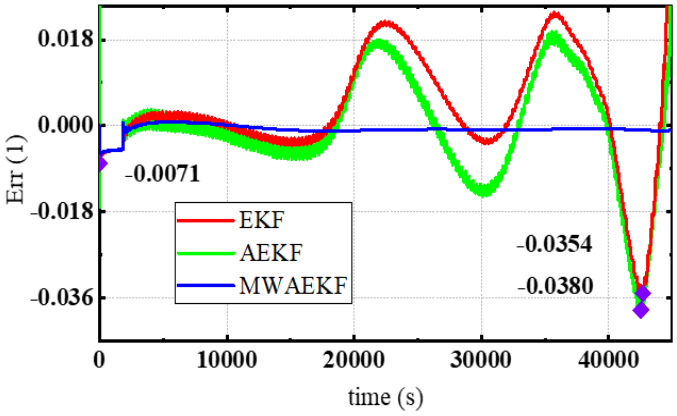

(a-2) Comparative SOC error results

(a) Gaussian observation noise $\boldsymbol{R}$ = 0 V/A

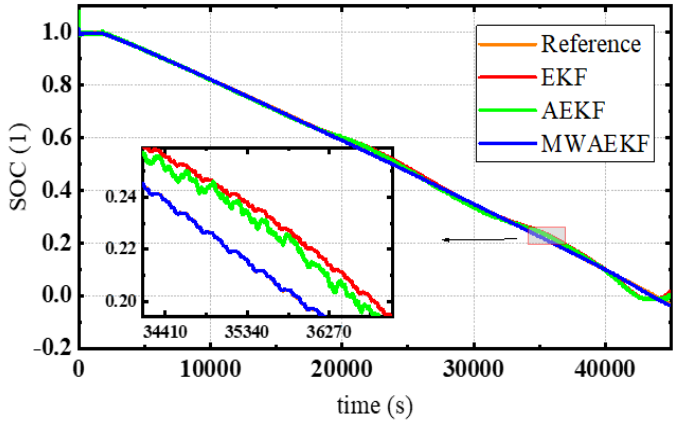

(b-1) Comparative SOC traction results

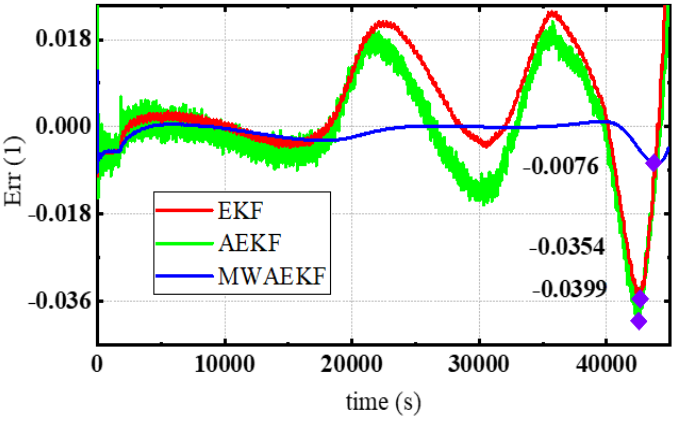

(b-2) Comparative SOC error results

(b) Gaussian observation noise $\boldsymbol{R}$ = 0.01 V/A

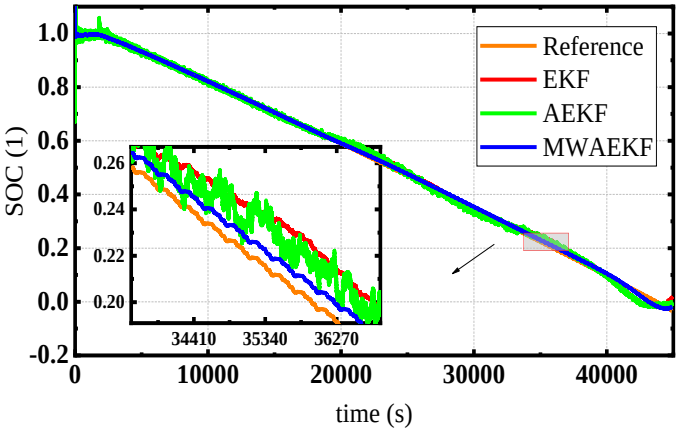

(c-1) Comparative SOC traction results

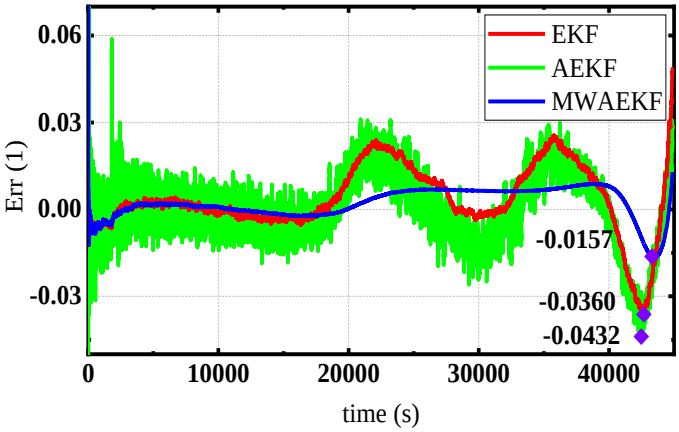

(c-2) Comparative SOC error results

(c) Gaussian observation noise $\boldsymbol{R}$ = 0.05 V/A

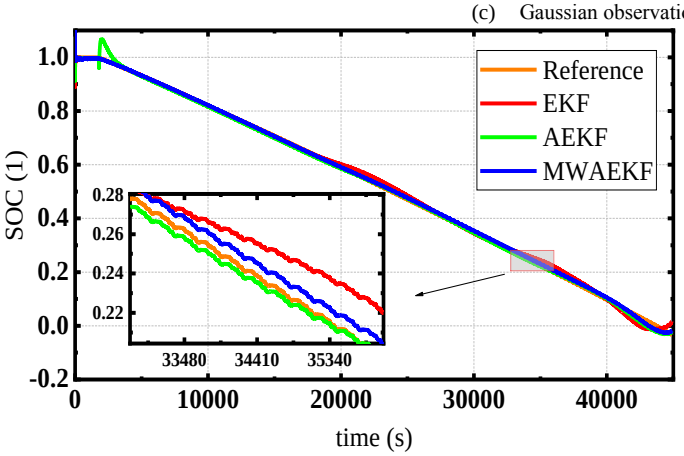

(d-1) Comparative SOC traction results

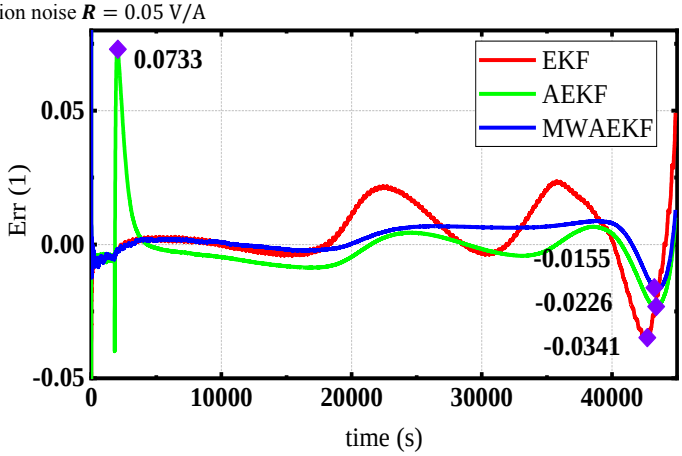

(d-2) Comparative SOC error results

(d) Colored noise $\boldsymbol{Q}$

Figure 11. Comparative SOC results using different noise interferences under the BBDST operating condition

As shown in Figure 11(a-1), without noise, it can be observed that even though the MWAEKF algorithm has poor initialization, it converges to the reference value more closely during the mid-stage of the estimation with low fluctuation amplitudes, showing a MAX of 0.71% compared to the EKF and AEKF algorithms, which have 3.54% and 3.80%, respectively. Also, when the noise is 0.01 V/A, the results show that the MWAEKF algorithm converges to the reference value more closely during the mid-stage of estimation with fewer fluctuations than the EKF and AEKF algorithms. Furthermore, when the noise is 0.05 V/A, the proposed MWAEKF algorithm has a MAX of 1.57% after fast convergence. However, the AEKF is further affected, where dense noise accumulates on the estimated results, causing the error to increase. This shows the excellent convergence characteristic of the MWAEKF algorithm and its good adaptability under the BBDST operating condition. Meanwhile, by comparing Figure 11 (d), it is known that when colored noise $\boldsymbol{Q}$ passes through the system, the estimation results of the MWAEKF algorithm are more stable than those of the EKF and AEKF algorithms. The results of the MWAEKF algorithm show a MAX of 1.55%, which is less than the EKF and AEKF algorithms, which are 3.41% and 2.26%, respectively. These prove that the proposed MWAEKF has good convergence characteristics under the BBDST operating condition with colored noise.

Further, it can be seen from Figures 11 (a)-(d) that with the progress of SOC estimation, the MWAEKF algorithm has a stable trend, while other algorithms have divergence problems after a long time of testing. The main possible reason is that for EKF and AEKF algorithms, with the progress of estimation with the interference noise, the error of the filter accumulates in the state variable, which causes the data saturation, and the error covariance matrix $\boldsymbol{P}$ is not robust, the process noise $\boldsymbol{R}$ and measurement noise $\boldsymbol{Q}$ cannot be updated properly, which resulting in the deterioration of SOC estimation accuracy. Meanwhile, the MWAEKF algorithm can not only reduce data saturation through the moving average method but also update noise variables. It can be seen that the update optimization of the MWAEKF outperforms the EKF and AEKF in correcting errors throughout the estimation process.. At the same time, with the increase of environmental noise, the estimation results of the state variables of the noise model also change in real-time, thus improving the accuracy of SOC estimation.

The SOC performance of the proposed MWAEKF algorithm is conducted and presented in comparison with the

EKF and AEKF algorithms using the MAE and RMSE metrics, as shown in Table 5.

Table 5. Performance evaluation results for different SOC algorithms under the BBDST operating condition

Noise interference	Metric	EKF	AEKF	MWAEKF
$\boldsymbol{R} = 0\ V/A$	RMSE	1.215%	1.1221%	0.1317%
	MAE	0.8496%	0.8222%	0.0933%
$\boldsymbol{R} = 0.01\ V/A$	RMSE	1.216%	1.1354%	0.2254%
	MAE	0.8501%	0.8342%	0.1373%
$\boldsymbol{R} = 0.05\ V/A$	RMSE	1.218%	1.237%	0.5638%
	MAE	0.8514%	0.9204%	0.4475%
$\boldsymbol{Q}$	RMSE	1.218%	1.022%	0.5638%
	MAE	0.8530%	0.6185%	0.4475%

As is shown in Table 5, using $\boldsymbol{R} = 0$ V/A, the RMSE for the proposed MWAEKF is only 0.1317%, which is less than the AEKF (1.1221%) and EKF (1.215%). Also, when the noise amplitude increases from 0.01 to 0.05 V/A, the RMSE for the MWAEKF algorithm increases from 0.2254% to 0.5638%, and that of the AEKF algorithm increases from 1.1354% to 1.237%. Overall, it can be observed that the MAEs and RMSEs show that the proposed MWAEKF algorithm outperforms both the EKF and AEKF algorithms with significant accuracy and robustness. The verification under BBDST operating conditions shows that the accuracy of SOC estimation using the MWAEKF algorithm has good performance under high noise conditions and great robustness.

4. Conclusion

The SOC estimation of the battery is susceptible to strong electromagnetic noise interference, leading to unstable and inaccurate estimations. Taking into account the problems caused by these noise uncertainties, the NBC-ECM is established based on a first-order Thevenin ECM to overcome the noise interferences and uncertainties by adding a system structure function to compensate for the noise interference. Then, an MWAEKF algorithm is proposed for SOC estimation, whose characteristic parameters use an SVD-BCRLS algorithm, and the results are compared to those of the EKF and AEKF algorithms using different system noise. The error comparison result shows that the SVD-BCRLS-MWAEKF algorithm provides optimal SOC estimation results. Using the proposed MWAEKF algorithm with a 0.05 V/A under the HPPC operating condition, the results show that the maximum SOC error is

1.3%, the RMSE is 0.3972%, and the MAE is 0.2316%. Under the BBDST operating condition, the maximum error of the proposed MWAEKF algorithm is 1.57%, the RMSE is 0.5638%, and the MAE is 0.4475%. The results of SOC estimation have high estimation accuracy under different operating conditions and noise interferences, demonstrating that the proposed MWAEKF algorithm can overcome the uncertainties encountered by lithium-ion batteries for real-time BMS applications.

In the future, the method of reducing the calculation amount of the SVD-BCRLS-MWAEKF calculation will be studied. We will also further study the applicability of the model due to the influence of noise caused by considering different ambient temperatures and aging factors for the state of health estimation of lithium-ion batteries.

Acknowledgments

The work is supported by the National Natural Science Foundation of China (Nos. 62173281), and the Natural Science Foundation of Sichuan Province (2023NSFSC1436).

References

1. Zhang, C., et al., *Energy storage system: Current studies on batteries and power condition system.* RENEWABLE & SUSTAINABLE ENERGY REVIEWS, 2018. **82**: p. 3091-3106.
2. Zhao, J., et al., *A review of system modeling, assessment and operational optimization for integrated energy systems.* Science China Information Sciences, 2021. **64**(9).
3. Ko, Y. and W. Choi, *A New SOC Estimation for LFP Batteries: Application in a 10 Ah Cell (HW 38120 L/S) as a Hysteresis Case Study.* Electronics, 2021. **10**(6): p. 705-719.
4. Kannayeram, G., N.B. Prakash, and R. Muniraj, *Intelligent hybrid controller for power flow management of PV/battery/FC/SC system in smart grid applications.* International Journal of Hydrogen Energy, 2020. **45**(41): p. 21779-21795.
5. Zhou, W., et al., *Review on the Battery Model and SOC Estimation Method.* Processes, 2021. **9**(9).
6. Rajaeifar, M.A., et al., *Challenges and recent developments in supply and value chains of electric vehicle batteries: A sustainability perspective.* RESOURCES CONSERVATION AND RECYCLING, 2022. **180**.
7. Trovo, A., *Battery management system for industrial-scale vanadium redox flow batteries: Features and operation.* Journal of Power Sources, 2020. **465**.
8. Wang, Y., et al., *A comprehensive review of battery modeling and state estimation approaches for advanced battery management systems.* Renewable and Sustainable Energy Reviews, 2020. **131**.
9. Tian, J., et al., *Battery state-of-charge estimation amid dynamic usage with physics-informed deep learning.* Energy Storage Materials, 2022. **50**: p. 718-729.
10. Hannan, M.A., et al., *A review of lithium-ion battery state of charge estimation and management system in electric vehicle applications: Challenges and recommendations.* Renewable and Sustainable Energy Reviews, 2017. **78**: p. 834-854.
11. Takyi-Aninakwa, P., et al., *An optimized relevant long short-term memory-squared gain extended Kalman filter for the state of charge estimation of lithium-ion batteries.* Energy, 2022. **260**: p. 1-15.
12. Hoque, M., et al., *Battery charge equalization controller in electric vehicle applications: A review.*

Renewable and Sustainable Energy Reviews, 2017. **75**: p. 1363-1385.
13. Takyi-Aninakwa, P., et al., *A hybrid probabilistic correction model for the state of charge estimation of lithium-ion batteries considering dynamic currents and temperatures.* Energy, 2023. **273**.
14. Ng, K.S., et al., *Enhanced coulomb counting method for estimating state-of-charge and state-of-health of lithium-ion batteries.* Applied Energy, 2009. **86**(9): p. 1506-1511.
15. Esser, M., G. Rohde, and C. Rehtanz, *Electrochemical Impedance Spectroscopy Setup based on Standard Measurement Equipment.* Journal of Power Sources, 2022. **544**.
16. Sun, L., G. Li, and F. You, *Combined internal resistance and state-of-charge estimation of lithium-ion battery based on extended state observer.* Renewable and Sustainable Energy Reviews, 2020. **131**.
17. Tang, X., et al., *A novel framework for Lithium-ion battery modeling considering uncertainties of temperature and aging.* Energy Conversion and Management, 2019. **180**: p. 162-170.
18. Lee, S., et al., *State-of-charge and capacity estimation of lithium-ion battery using a new open-circuit voltage versus state-of-charge.* Journal of power sources, 2008. **185**(2): p. 1367-1373.
19. Lai, X., Y.J. Zheng, and T. Sun, *A comparative study of different equivalent circuit models for estimating state-of-charge of lithium-ion batteries.* Electrochimica Acta, 2018. **259**: p. 566-577.
20. Chen, J., et al., *State of charge estimation of lithium-ion battery using denoising autoencoder and gated recurrent unit recurrent neural network.* Energy, 2021. **227**.
21. Takyi-Aninakwa, P., et al., *An optimized long short-term memory-weighted fading extended Kalman filtering model with wide temperature adaptation for the state of charge estimation of lithium-ion batteries.* Applied Energy, 2022. **326**.
22. Wang, Q., et al., *Deep convolutional neural network based closed-loop SOC estimation for lithium-ion batteries in hierarchical scenarios.* Energy, 2022. **261**(125718).
23. Li, H., et al., *A novel state of charge estimation for energy storage systems based on the joint NARX network and filter algorithm.* International Journal of Electrochemical Science, 2021. **16**.
24. Hossain Lipu, M.S., et al., *Data-driven state of charge estimation of lithium-ion batteries: Algorithms, implementation factors, limitations and future trends.* Journal of Cleaner Production, 2020. **277**.
25. Xi, Z., et al., *Accurate and reliable state of charge estimation of lithium ion batteries using time-delayed recurrent neural networks through the identification of overexcited neurons.* Applied Energy, 2022. **305**.
26. Lai, X., Y. Zheng, and T. Sun, *A comparative study of different equivalent circuit models for estimating state-of-charge of lithium-ion batteries.* Electrochimica Acta, 2018. **259**: p. 566-577.
27. Hu, X., et al., *Battery Lifetime Prognostics.* Joule, 2020. **4**(2): p. 310-346.
28. Wu, L.X., et al., *Online SOC Estimation Based on Simplified Electrochemical Model for Lithium-Ion Batteries Considering Current Bias.* Energies, 2021. **14**(17): p. 1-11.
29. Luo, K., et al., *A review of deep learning approach to predicting the state of health and state of charge of lithium-ion batteries.* Journal of Energy Chemistry, 2022. **74**: p. 159-173.
30. Wang, Q., et al., *Correlation between the model accuracy and model-based SOC estimation.* Electrochimica Acta, 2017. **228**: p. 146-159.
31. Takyi-Aninakwa, P., et al., *Enhanced multi-state estimation methods for lithium-ion batteries considering temperature uncertainties.* Journal of Energy Storage, 2023. **66**.
32. Takyi-Aninakwa, P., et al., *A strong tracking adaptive fading-extended Kalman filter for the state of charge estimation of lithium-ion batteries.* Int J Energy Res. , 2022. **46**(12): p. 16427-16444.
33. Nian, P., Z. Shuzhi, and Z. Xiongwen, *Co-estimation for capacity and state of charge for lithium-ion batteries using improved adaptive extended Kalman filter.* Journal of Energy Storage, 2021. **40**.
34. Lin, X. and A.G. Stefanopoulou, *Analytic Bound on Accuracy of Battery State and Parameter Estimation.* Journal of The Electrochemical Society, 2015. **162**(9): p. A1879-A1891.
35. Chen, P., et al., *Evaluation of Various Offline and Online ECM Parameter Identification Methods of Lithium-*

Ion Batteries in Underwater Vehicles. ACS Omega, 2022. **7**(34): p. 30504-30518.
36. Fleischer, C., et al., *On-line adaptive battery impedance parameter and state estimation considering physical principles in reduced order equivalent circuit battery models part 2. Parameter and state estimation.* Journal of Power Sources, 2014. **262**: p. 457-482.
37. He, Z., et al., *Adaptive state of charge estimation for Li-ion batteries based on an unscented Kalman filter with an enhanced battery model.* Energies, 2013. **6**(8): p. 4134-4151.
38. Sun, F., et al., *Adaptive unscented Kalman filtering for state of charge estimation of a lithium-ion battery for electric vehicles.* Energy, 2011. **36**(5): p. 3531-3540.
39. Qi, C., et al., *An improved adaptive spherical unscented Kalman filtering method for the accurate state-of-charge estimation of lithium-ion batteries.* International Journal of Circuit Theory and Applications, 2022.
40. Xia, B., et al., *State of Charge Estimation of Lithium-Ion Batteries Using an Adaptive Cubature Kalman Filter.* Energies, 2015. **8**(6): p. 5916-5936.
41. Plett, G.L., *Sigma-point Kalman filtering for battery management systems of LiPB-based HEV battery packs: Part 1: Introduction and state estimation.* Journal of Power Sources, 2006. **161**(2): p. 1356-1368.
42. Khan, H.F., et al., *A Lagrange multiplier and sigma point Kalman filter based fused methodology for online state of charge estimation of lithium-ion batteries.* Journal of Energy Storage, 2021. **41**: p. 1-13.
43. He, H., et al., *State-of-charge estimation of the lithium-ion battery using an adaptive extended Kalman filter based on an improved Thevenin model.* IEEE Transactions on vehicular technology, 2011. **60**(4): p. 1461-1469.
44. Peng, N., et al., *Online parameters identification and state of charge estimation for lithium-ion batteries using improved adaptive dual unscented Kalman filter.* International Journal of Energy Research, 2020. **45**(1): p. 975-990.
45. Li, J., et al., *Sequential Monte Carlo filter for state estimation of LiFePO 4 batteries based on an online updated model.* Journal of Power Sources, 2014. **247**: p. 156-162.
46. Tong, Y., et al., *Improved unscented Kalman filter for state of charge estimation of lithium-ion battery with one-step randomly measurement loss and inaccurate noise covariance matrices.* Digital Signal Processing, 2022. **131**.
47. Bhattacharyya, H.S., A.B. Choudhury, and C.K. Chanda, *On-road estimation of state of charge of lithium-ion battery by extended and dual extended Kalman filter considering sensor bias.* International Journal of Energy Research, 2022. **46**(11): p. 15182-15197.
48. Xu, C., et al., *Dual fuzzy-based adaptive extended Kalman filter for state of charge estimation of liquid metal battery.* Applied Energy, 2022. **327**.
49. Maheshwari, A. and S. Nageswari, *Real-time state of charge estimation for electric vehicle power batteries using optimized filter.* Energy, 2022. **254**.
50. Xi, Z., et al., *Learning of Battery Model Bias for Effective State of Charge Estimation of Lithium-Ion Batteries.* IEEE Transactions on Vehicular Technology, 2019. **68**(9): p. 8613-8628.
51. Wang, Y.J., et al., *A comprehensive review of battery modeling and state estimation approaches for advanced battery management systems.* Renewable & Sustainable Energy Reviews, 2020. **131**(110015): p. 1-23.